2015

# Analysis of the Tapered Transition Waveguide

Ryan J. Shaver
*Wright State University*

# Analysis of the Tapered Transition Waveguide

A thesis submitted in partial fulfillment of the
requirements for the degree of
Master of Science in Engineering

By

RYAN SHAVER
B.S., Wright State University 2012

2015

Wright State University

WRIGHT STATE UNIVERSITY

GRADUATE SCHOOL

May 1, 2015

I HEREBY RECOMMEND THAT THE THESIS PREPARED UNDER MY SUPERVISION BY Ryan Shaver ENTITLED Analysis of Tapered Transition Waveguide BE ACCEPTED IN PARTIAL FULFILLMENT OF THE REQUIREMENTS FOR THE DEGREE OF Master of Science in Engineering.

Michael A. Saville, Ph.D., P.E.
Thesis Director

Brian D. Rigling, Ph.D.
Chair, Department of Electrical Engineering

Committee on
Final Examination

Michael A. Saville, Ph.D., P.E.

Brian Rigling, Ph.D.

Yan Zhuang, Ph.D

Robert E. W. Fyffe, Ph.D.
Vice President for Research and
Dean of the Graduate School

# ABSTRACT

Shaver, Ryan. M.S.Egr. Department of Electrical Engineering, Wright State University, 2015. Analysis of the Tapered Transition Waveguide.

The tapered transition waveguide is used in waveguide measurement systems for characterizing biaxial electromagnetic properties of materials, but its complex geometry does not support an analytic field solution. To ensure single-mode field behavior, the system includes sections of standard waveguides that only support the dominant mode. As a result, full-wave modeling and simulation of the system is exceedingly large.

Using the finite-element method to analyze the high-order modes at the junctions and to explore field configurations within the transition altering geometry, it is shown that besides the $TE_{10}$ mode, the $TE_{11}$ mode is significant. Then, two methods are proposed for using multi-mode excitation in the model as a way to simulate the scattering parameters of a material without the feed and transition section.

## Contents

**LIST OF FIGURES**

**LIST OF TABLES**

## ACKNOWLEDGMENT

I would like to thank my family, friends, and thesis advisor for all the support during my education.

# CHAPTER 1

# INTRODUCTION

## 1.1. Motivation

With advancements in material science and fabrication techniques, the fields of antenna and microwave engineering have the new opportunity to use precise man-made materials. By using tailored materials, one could design array antennas with reduced elemental coupling, or guiding structures with lower insertion loss. Anisotropic materials offer additional degrees of freedom in the constitutive parameters over isotropic materials, but require a 3x3 tensor for both the permittivity and permeability [4][5]. As anisotropic materials are very difficult to fabricate for wide-band operation, a simpler approach would be to design biaxial materials and build up to fully anisotropic materials. In fact, this work is inspired by recent works on the measurement of the scattering matrix of biaxial samples in waveguide test fixtures (Figure 1). In those methods, different waveguide sections are studied and analyzed to understand how to minimize the effects of higher-order modes that result from abrupt changes in the waveguide at the junctions between the excitation port, sample region, and transmission port.

## 1.2. Challenges

The anisotropic nature of the biaxial material requires an individual to model, design, and characterize the material along all three principal axes. This attribute can be

seen in the biaxially anisotropic representation for the permittivity, $\bar{\bar{\varepsilon}}$, and the permeability, $\bar{\bar{\mu}}$, as shown in equations (1.2.1) and (1.2.2)

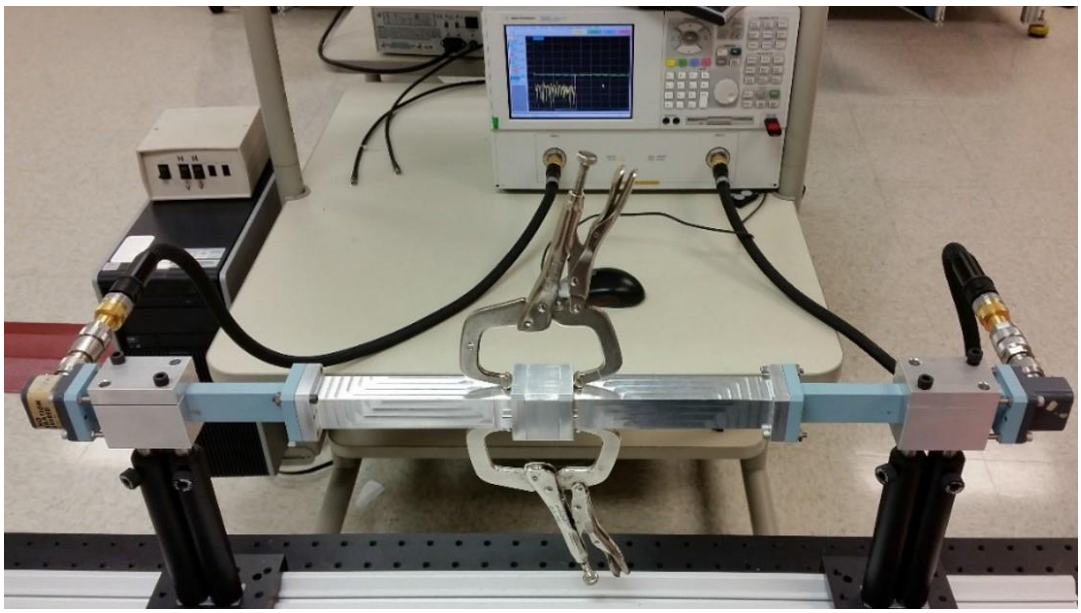

Figure 1 Waveguide test fixture in [1].

$$\bar{\bar{\varepsilon}} = \begin{bmatrix} \varepsilon_{xx} & 0 & 0 \\ 0 & \varepsilon_{yy} & 0 \\ 0 & 0 & \varepsilon_{zz} \end{bmatrix} \tag{1.2.1}$$

$$\bar{\bar{\mu}} = \begin{bmatrix} \mu_{xx} & 0 & 0 \\ 0 & \mu_{yy} & 0 \\ 0 & 0 & \mu_{zz} \end{bmatrix} \tag{1.2.2}$$

which relate the electric ($\vec{D}$) and magnetic ($\vec{B}$) fluxes to the fields $\vec{E}$ and $\vec{H}$, respectively as

$$\vec{D} = \bar{\bar{\varepsilon}}\vec{E} \tag{1.2.3}$$

$$\vec{B} = \bar{\bar{\mu}}\vec{H} \tag{1.2.4}$$

The flux magnitudes are proportional to the field magnitudes, but fluxes are not polarized with the fields in anisotropic media. Therefore, material characterization involves multiple measurements based upon which axis is being excited, and which material property is to be estimated from the measurement. From [5], four different measurement orientations are needed to fully characterize a biaxial sample with the waveguide system. In a design cycle where many different configurations of the test sample are needed in order to determine the optimal configuration, one would need to fabricate and measure many test samples. Measurements have error sources, but fabrication can also pose additional error. During prototyping, it is helpful to have a way to exclude measurement or fabrication error sources. The most common alternative is to use full-wave modeling and simulation as a surrogate for the actual measurement system. Then, measurement and fabrication errors are traded for computational errors and time to compute. Although computational error is controllable, there is a significant trade-off between simulation accuracy and computation time.

The primary challenge is the size of the numerical problem. The computer aided design (CAD) model must be meshed on the order of a tenth of a wavelength and for the transition guide shown in Figure 1, there are over 90,000 unknowns in the underlying matrix problem. Each simulation can vary from tens of minutes to multiple hours to compute. Therefore, efficiency in the simulation method is the primary roadblock to simulation of thousands of iterations needed for design.

In addition, the waveguide junctions cause spurious responses and higher-order modes within different regions of the guide [10]. Each waveguide section has a different geometrical shape and results in a different cut-off frequency and distinct and discrete electric field behaviors referred to as modes. These modes exist at or above the fundamental $TE_{10}$ mode and give rise to the undesired, or spurious, modes that can affect simulation. Additionally, the scale and dimensions of the waveguide vary with respect to the sample; thus, making the numerical mesh more complicated than a bulk material isotropic sample. Small geometric features of the test material and large dimensions of the guide pose a multi-scale geometry model. Also, the physical length of the guide makes the problem numerically large and requires a lot of computing resources and solution time. Full wave simulations can calculate a solution, but the time and memory may be too large or the accuracy may be degraded because of the geometry model.

### 1.3. Research Hypothesis

This work proposes an alternate approach to full wave simulation of the complete system shown in Figure 1. Instead, full wave simulations are carried out on each waveguide segment except for the sample region. Electromagnetic scattering matrices are calculated for each section of waveguide and stored. Then, using $TE_{10}$ excitation with the scattering parameters, the excitation can be specified directly at the port of sample. Only the sample region is iteratively simulated to optimize the biaxial material design.

This approach would alleviate the need to simulate the long transition sections and would significantly decrease simulation time.

The approach is presented for the case of WR-90 rectangular waveguide and the tapered transition section shown in Figure 1. Finite element method is used to perform the full-wave simulation to compute scattering parameters and modal expansion of the fields is used to formulate the fields at the sample region. Lastly, the technique is outlined for how it can be used to optimize the design parameters of the Knisely crystal [1].

### 1.4. Thesis Outline

Chapter II presents a survey of related computational methods and scattering matrix to transmission matrix methods. Chapter III describes the approach to model biaxial samples using finite element method and verifies the transmission matrix representation. Chapter IV presents results of the fields before and after the T-matrix to the sample. Chapter V offers conclusions and recommendations for future work.

# CHAPTER 2

# BACKGROUND

## 2.1. Previous work

The work presented in this thesis is inspired by [1], where Kinsley and Havrilla presented an analysis of the rectangular to square transition (RTST) measurement system for characterizing electromagnetic material properties. The system in [1] is shown in Figure 2, where the yellow cubic region holds the material under test. The cubic dimension allows rotation about the principal axes so the waveguide system can measure selected material tensor quantities.

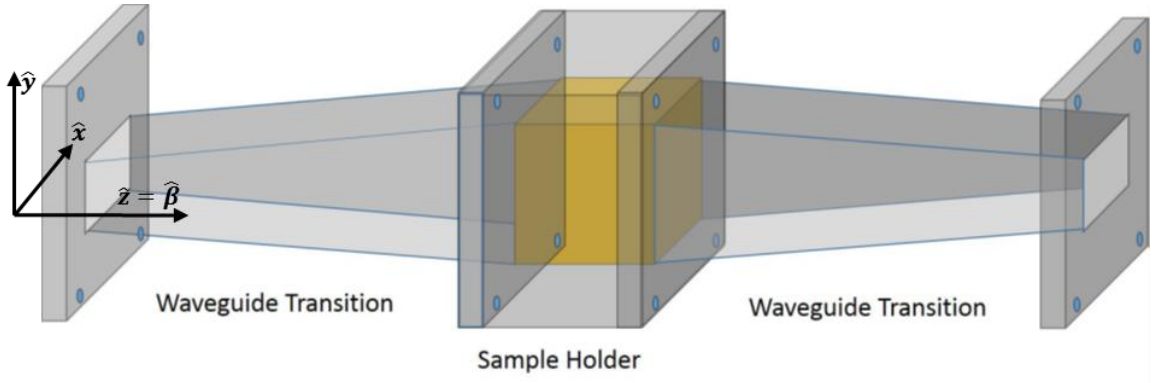


Figure 2. Waveguide measurement system from Kinsley and Havrilla [1].

Constitutive parameter extraction of [1] is based on matching boundary conditions at each junction in the waveguide system to solve for the fields and then fitting to a parametric model consisting of the design variables for the material under test. As the

sample is cubic, the sample can be characterized from six different measurements corresponding to the six possible orientations of the test fixture. Each orientation of the sample is excited by the $TE_{10}$ excitation**.**

The parametric model is also based upon the PEC (perfectly electrically conductive) nature of the waveguide test fixture. The tangential electric fields must be zero at the PEC wall. Furthermore, when only a $TE_{10}$ mode is induced within the test fixture, the curl equations are invariant to the field direction and we can represent all the fields within the guide by transverse electric (TE) and transverse magnetic (TM) solutions to Maxwells Equations.

$$\nabla \times \vec{E} = -j\omega\bar{\bar{\mu}}\vec{H} \tag{2.1.1}$$

$$\nabla \times \vec{H} = j\omega\bar{\bar{\varepsilon}}\vec{E} \tag{2.1.2}$$

For $TE_{10}$ mode excitation, only TE modes exist and (2.1.1) and (2.1.2) reduce to:

$$\frac{\partial E_y}{\partial z} = j\omega\mu_x H_x \tag{2.1.3}$$

$$\frac{\partial E_y}{\partial x} = -j\omega\mu_z H_z \tag{2.1.4}$$

$$\frac{\partial H_z}{\partial x} - \frac{\partial H_z}{\partial z} = -j\omega\varepsilon_y E_y \tag{2.1.5}$$

When equations (2.1.3) and (2.1.4) are substituted into (2.1.5), the $TE_z$ wave equation within the guide becomes

$$\frac{\mu_x}{\mu_z}\frac{\partial^2 E_y(x,z)}{\partial x^2} + \frac{\partial^2 E_y(x,z)}{\partial z^2} = -\omega^2 \mu_x \varepsilon_y E_y(x,z) \tag{2.1.6}$$

Equation (2.1.6) is not trivial to solve, but finite element method makes it tenable [13][14]. Further work in this thesis aims to reduce the computation times needed to simulate and analyze this tapered test fixture along with the de-embedding of *S*-parameter values measured from the biaxial anisotropic sample.

## 2.2. De-embedding

The scattering parameters computed from the FEM solution to (2.1.6) relate complex amplitudes (magnitude and phase) of the traveling waves within the RTST test fixture to a specific phase reference within the guide. Consider the two port network seen in Figure 3 where the original terminal planes are assumed to be Port 1 and Port 2 (in blue). If the scattering parameters are found for the system, $\bar{S}$, and we wish to consider a new reference plane at location further down the length of the transmission line, we will yield a new scattering matrix represented as $\bar{S}'$.

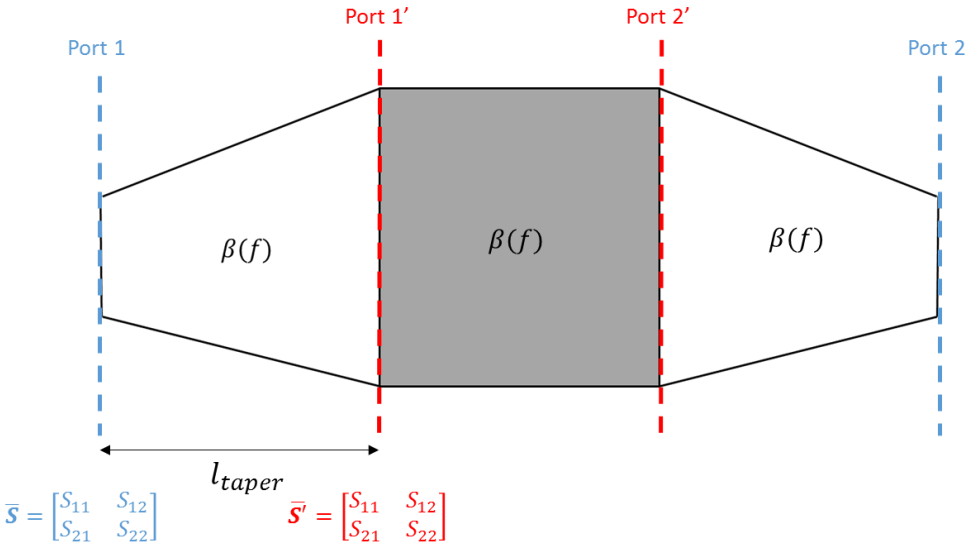


Figure 3. Shifted reference plane for transition waveguide section.

If we consider the incident and reflected voltage waves at each port, and follow the discussion on shifted reference planes by Pozar [3], we can solve for the new scattering parameters at a distance $l_{taper}$ (in this example) from the original terminal planes.

The *S*-parameters, or scattering matrix, simply relate incoming waves to outgoing waves. For a two-port system represented by Figure 4, the *S*-parameters are defined by equations (2.2.1) through (2.2.5).

$$\begin{bmatrix} b_1 \\ b_2 \end{bmatrix} = \begin{bmatrix} S_{11} & S_{12} \\ S_{21} & S_{22} \end{bmatrix} \begin{bmatrix} a_1 \\ a_2 \end{bmatrix} \tag{2.2.1}$$

$$S_{11} = \left. \frac{b_1}{a_1} \right|_{a_2=0} \tag{2.2.2}$$

$$S_{12} = \frac{b_1}{a_2}\Big|_{a_1=0} \tag{2.2.3}$$

$$S_{21} = \frac{b_2}{a_1}\Big|_{a_2=0} \tag{2.2.4}$$

$$S_{22} = \frac{b_2}{a_2}\Big|_{a_1=0} \tag{2.2.5}$$

where $a_1, a_2$ and $b_1, b_2$ represent incoming and outgoing waves at the ports, respectively. It is important to note that the *S* parameters are defined at the unprimed ports of Figure 3. Assuming lossless waveguide, the parameters are easily related to a different reference plane, e.g., primed plane in Figure 4, when the propagation constant is known. This process is known as the de-embed process and is useful for measurement test fixtures that require additional transmission lines to accommodate the device under test.

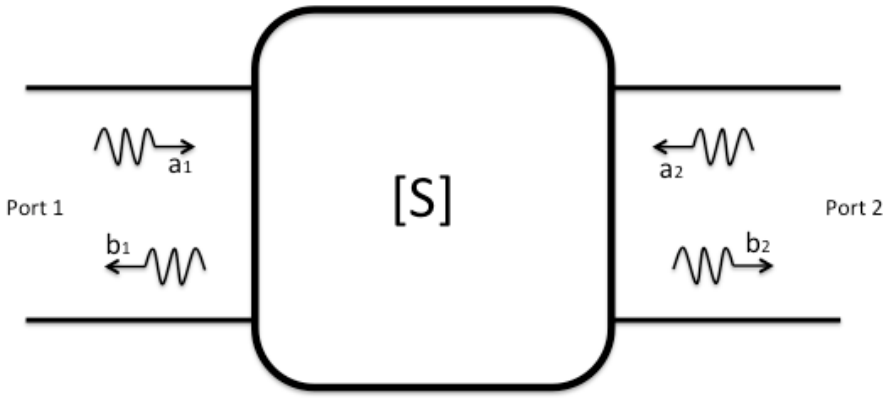


Figure 4. Two-port network *S*-matrix representation

When the wave propagation constant is known in lossless guide, the scattering parameters at the new reference plane can be calculated as

$$\bar{S}' = \begin{bmatrix} 0 & e^{-j2\beta l} \\ -e^{-j2\beta l} & 0 \end{bmatrix} \bar{S} \tag{2.2.6}$$

where $\beta$ is the propagation constant and $l$ is the length of the transmission line. If the line is lossless, it will only induce a phase shift corresponding to the electrical length the wave must travel. Equation (2.2.6) makes good physical sense because the wave travels twice the distance $l$ (forward and backward).

### 2.3. *T*-matrix formation

The transfer matrix, or *T*-matrix, directly relates the waves on the input port to that on the output port and is much more convenient for analyzing cascaded microwave circuits. *S*-parameters relate incoming waves to outgoing waves while *T*-parameters relate incoming and outgoing waves at Port 1 to incoming and outgoing waves at Port 2. For incoming ($\vec{a}$) and outgoing ($\vec{b}$) waves, the *T*-matrix expression is

$$\begin{bmatrix} a_1 \\ b_1 \end{bmatrix} = \begin{bmatrix} T_{11} & T_{12} \\ T_{21} & T_{22} \end{bmatrix} \begin{bmatrix} b_2 \\ a_2 \end{bmatrix} \tag{2.3.1}$$

If we can characterize each individual segment of the RTST guide, we will be able to excite the test fixture directly at Port $1'$. This new port excitation will be incident on the sample region instead of the entire test fixture, thus eliminating the need to model the transition guide and drastically reducing computation times for the numerical FEM

approach. The *T*-matrix simply links the incoming and outgoing waves in a manner different than the *S*-matrix. One may convert between the two representations as in equations (2.3.2) through (2.3.5) as long as the scattering matrix is defined as (2.2.1) [6].

$$T_{11} = \frac{1}{S_{21}} \tag{2.3.2}$$

$$T_{12} = -\frac{S_{22}}{S_{21}} \tag{2.3.3}$$

$$T_{21} = \frac{S_{11}}{S_{21}} \tag{2.3.4}$$

$$T_{22} = \frac{S_{12}S_{21} - S_{11}S_{22}}{S_{21}} \tag{2.3.5}$$

If there are multiple transmission line segments which have already been characterized in terms of the incoming ($\vec{a} = [a_1, a_2]^T$) and outgoing ($\vec{b} = [b_1, b_2]^T$) waves, then each has a *T*-matrix and the response of the cascaded network can be represented by matrix multiplication of the *T* matrices. In Figure 5, each waveguide section has an individual scattering matrix representation. Each individual scattering matrix is converted into its corresponding *T*-matrix following equations (2.3.2) through (2.3.5). With each *T*-matrix calculated, one can model the incoming and outgoing complex wave amplitudes at an arbitrary reference plane.

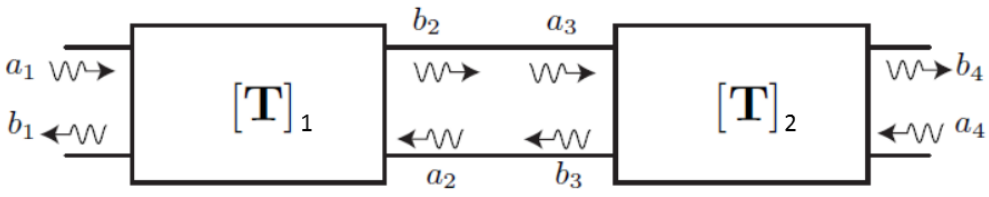


Figure 5. *T*-matrix representation of a cascaded network [15].

For any $M$ number of waveguide segments, the total *T*-matrix can be calculated by doing a "left-to-right" multiplication in the direction of the forward going wave from Port 1.

$$\begin{bmatrix} a_1 \\ b_1 \end{bmatrix} = T_1 \begin{bmatrix} b_2 \\ a_2 \end{bmatrix} = T_1 \begin{bmatrix} a_3 \\ b_3 \end{bmatrix} = T_1 T_2 \begin{bmatrix} a_4 \\ b_4 \end{bmatrix} \tag{2.3.6}$$

$$T_M = T_1 T_2 \dots T_m \tag{2.3.7}$$

After calculating the overall *T*-matrix, then the *S*-parameters are computed for the overall system as [6]

$$S_{11} = \frac{T_{21}}{T_{11}} \tag{2.3.8}$$

$$S_{12} = \frac{T_{11}T_{22} - T_{12}T_{21}}{T_{11}} \tag{2.3.9}$$

$$S_{21} = \frac{1}{T_{11}} \tag{2.3.10}$$

$$S_{22} = -\frac{T_{12}}{T_{11}} \tag{2.3.11}$$

For a reciprocal network, the *T*-parameters must follow the condition [15]:

$$T_{11}T_{22} - T_{12}T_{21} = 1 \tag{2.3.12}$$

## 2.4. Mode Matching

Electromagnetic wave propagation in waveguides is well-known for rectangular and square guides [3],[4]. When multiple sections of guide vary in size or material, boundary conditions cause complicated field behavior. A common method to analyze the fields inside any section of guide is known as mode matching [5],[13]. This approach utilizes linear superposition to express the total fields within the guide as a summation of all possible modes which can exist in the cross section of the guide. These cross-sectional fields are represented by a set of eigen-functions which correspond to the physical geometry of the section, and are solved by satisfying Maxwell's equations within each section. Maxwell's equations are satisfied by equating boundary conditions and preserving orthogonality of the eigen-functions at each junction. In other words, the fields on both sides of the junction discontinuity are expanded in terms of the modes in the respective regions with unknown coefficients [16]. Figure 6 represents a guide with three different sections, each *n*th section has its own set of electric $\vec{e}_m^{(n)}$and magnetic $\vec{h}_m^{(n)}$ eigenfunctions, propagation constants $\beta_m^{(n)}$, and wave impedances $Z_m^{(n)}$ per $m$ mode.

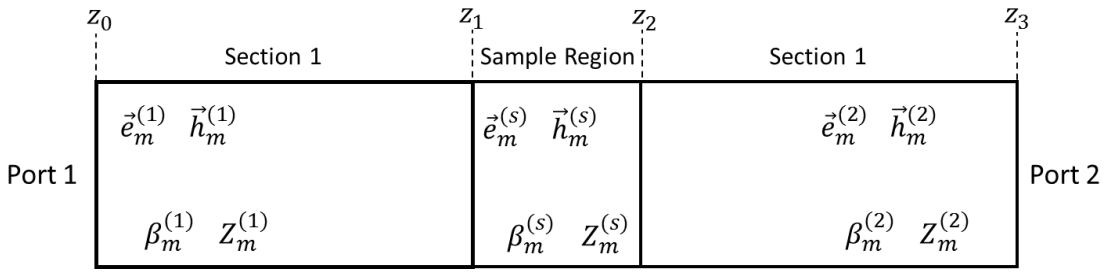


Figure 6. Waveguide sections with boundaries at the ports and sample-guide interfaces.

The total fields in each waveguide section must account for all modes. As each of the three sections of Figure 6 has a different electromagnetic response based upon its geometry and material parameters, the fields are

$$\vec{E}^{(1)}(x,y,\mathrm{z} \le z_1) = \sum_{m=1}^{P} A_m^{+}\vec{e}_m^{(1)}(x,y)e^{-j\beta_m^{(1)}z} + \sum_{m=1}^{\infty} A_m^{-}\vec{e}_m^{(1)}(x,y)e^{+j\beta_m^{(1)}z} \tag{2.4.1}$$

$$\vec{H}^{(1)}(x,y,\mathrm{z} \le z_1) = \sum_{m=1}^{P} A_m^{+}\vec{h}_m^{(1)}(x,y)e^{-j\beta_m^{(1)}z} - \sum_{m=1}^{\infty} A_m^{-}\vec{h}_m^{(1)}(x,y)e^{+j\beta_m^{(1)}z} \tag{2.4.2}$$

$$\vec{E}^{(s)}(x,y,z_1 \le z \le z_2) = \sum_{m=1}^{\infty} B_m^{+}\vec{e}_m^{(s)}(x,y)e^{-j\beta_m^{(s)}z} + \sum_{m=1}^{\infty} B_m^{-}\vec{e}_m^{(s)}(x,y)e^{+j\beta_m^{(s)}z} \tag{2.4.3}$$

$$\vec{H}^{(s)}(x,y,z_1 \le z \le z_2) = \sum_{m=1}^{\infty} B_m^{+}\vec{h}_m^{(s)}(x,y)e^{-j\beta_m^{(s)}z} - \sum_{m=1}^{\infty} B_m^{-}\vec{h}_m^{(s)}(x,y)e^{+j\beta_m^{(s)}z} \tag{2.4.4}$$

$$\vec{E}^{(2)}(x,y,z_2 \le z) = \sum_{m=1}^{\infty} C_m^{+}\vec{e}_m^{(2)}(x,y)e^{-j\beta_m^{(2)}z} + \sum_{m=1}^{\infty} C_m^{-}\vec{e}_m^{(2)}(x,y)e^{+j\beta_m^{(2)}z} \tag{2.4.5}$$

$$\vec{H}^{(2)}(x,y,z_2 \le z) = \sum_{m=1}^{\infty} C_m^{+}\vec{h}_m^{(2)}(x,y)e^{-j\beta_m^{(2)}z} - \sum_{m=1}^{\infty} C_m^{-}\vec{h}_m^{(2)}(x,y)e^{+j\beta_m^{(2)}z} \tag{2.4.6}$$

where the forward-going (+) and backward-going (-) coefficients are

$A_m^+, A_m^-, B_m^+, B_m^-, C_m^+, C_m^-$, and the wave functions in each region are

$$\vec{e}_m^{(1)}(x,y) = \hat{y}\sin(k_{x,m}^{(1)}x) \tag{2.4.7}$$

$$\vec{h}_m^{(1)}(x,y) = \hat{x}\frac{1}{Z_m^{(1)}}\sin(k_{x,m}^{(1)}x) \tag{2.4.8}$$

$$\vec{e}_m^{(s)}(x,y) = \hat{y}\sin(k_{x,m}^{(s)}x) \tag{2.4.9}$$

$$\vec{h}_m^{(s)}(x,y) = \hat{x}\frac{1}{Z_m^{(s)}}\sin(k_{x,m}^{(s)}x) \tag{2.4.10}$$

$$\vec{e}_m^{(2)}(x,y) = \hat{y}\sin(k_{x,m}^{(2)}x) \tag{2.4.11}$$

$$\vec{h}_m^{(2)}(x,y) = \hat{x}\frac{1}{Z_m^{(2)}}\sin(k_{x,m}^{(2)}x) \tag{2.4.12}$$

and the wave propagation constants and impedances are [4],[5]

$$k_{x,m}^{(1)} = \frac{\pi}{w_1}m, \qquad m = 1,\dots,P \tag{2.4.13}$$

$$k_{x,m}^{(s)} = \frac{\pi}{w_s}m, \qquad m = 1,\dots,P \tag{2.4.14}$$

$$k_{x,m}^{(2)} = \frac{\pi}{w_2}m, \qquad m = 1,\dots,P \tag{2.4.15}$$

$$\beta_m^{(1)} = \sqrt{k^2 - \left(k_{x,m}^{(1)}\right)^2} = \pm\beta_{r,m}^{(1)} \pm \beta_{i,m}^{(1)} \tag{2.4.16}$$

$$\beta_m^{(s)} = \sqrt{k^2 - \left(k_{x,m}^{(s)}\right)^2} = \pm\beta_{r,m}^{(s)} \pm \beta_{i,m}^{(s)} \tag{2.4.17}$$

$$\beta_m^{(2)} = \sqrt{k^2 - \left(k_{x,m}^{(2)}\right)^2} = \pm\beta_{r,m}^{(2)} \pm \beta_{i,m}^{(2)} \tag{2.4.18}$$

The square root operations result in complex-valued propagation constants. Hence, the constants are selected according to the direction of the wave such that only propagating and evanescing waves can exist. In other words, waves cannot grow because there are no intrinsic sources of energy in the system.

For transverse-electric (TE) field excitation used in the waveguide measurement system, the wave impedances are

$$Z_m^{(1)} = \frac{\eta^{(1)}}{\sqrt{1 - \left(\frac{\beta_m^{(1)}}{k^{(1)}}\right)^2}} \tag{2.4.19}$$

$$Z_m^{(s)} = \frac{\eta^{(s)}}{\sqrt{1 - \left(\frac{\beta_m^{(s)}}{k^{(s)}}\right)^2}} \tag{2.4.20}$$

$$Z_m^{(2)} = \frac{\eta^{(2)}}{\sqrt{1 - \left(\frac{\beta_m^{(2)}}{k^{(2)}}\right)^2}} \tag{2.4.21}$$

where $k^{(1)} = 2\pi f\sqrt{\mu_1\epsilon_1}$, $k^{(2)} = 2\pi f\sqrt{\mu_2\epsilon_2}$, and $k^{(s)} = 2\pi f\sqrt{\mu_{xx}\epsilon_{yy}}$ for the biaxial sample material. Also, $\eta^{(1)} = \sqrt{\mu_1/\epsilon_1}$, $\eta^{(2)} = \sqrt{\mu_2/\epsilon_2}$, and $\eta^{(s)} = \sqrt{\mu_{xx}/\epsilon_{yy}}$.

To determine the total fields inside the guide, equations (2.4.1) through (2.4.6) are evaluated to enforce boundary conditions for the electric and magnetic fields. The total fields are matched at each junction represented by equations (2.4.22) through (2.4.25)

$$\hat{z} \times \vec{E}^{(1)}(x, y, z_1) = \hat{z} \times \vec{E}^{(s)}(x, y, z_1) \tag{2.4.22}$$

$$\hat{z} \times \vec{H}^{(1)}(x, y, z_1) = \hat{z} \times \vec{H}^{(s)}(x, y, z_1) \tag{2.4.23}$$

$$\hat{z} \times \vec{E}^{(s)}(x, y, z_2) = \hat{z} \times \vec{E}^{(2)}(x, y, z_2) \tag{2.4.24}$$

$$\hat{z} \times \vec{H}^{(s)}(x, y, z_2) = \hat{z} \times \vec{H}^{(2)}(x, y, z_2) \tag{2.4.25}$$

Once these relations are made, linear matrix algebra can be used to determine the coefficients $A_m^{-/+}$, $B_m^{-/+}$, and $C_m^{-/+}$. The coefficients are then used to compute the scattering matrix. Since the excitation port is assumed to be perfectly matched, no higher-order forward going waves will be present in section 1 ($A_m^+ = A_1^+$). Also, the transmission port is perfectly matched so that no reflected waves will exist in section 2 ($C_m^- = 0$).

Lastly, the *S*-parameters simply relate the incoming and outgoing waves at the ports. For excitation by the *p*th mode

$$S_{11}(p) = \frac{\sum_{m=1}^{\infty} A_m^-}{A_p^+} \tag{2.4.11}$$

$$S_{21}(p) = \frac{\sum_{m=1}^{\infty} C_m^+}{A_p^+} \tag{2.4.12}$$

Once a mode matching solution can be obtained, we can use the numerical solutions data to construct an iterative constitutive parameter extraction technique. This stems from the fact that $A_p^+$, $\vec{e}_m^{(1)}, \vec{h}_m^{(1)}, \vec{e}_m^{(2)}, \vec{h}_m^{(2)}, \beta_m^{(1)}, Z_m^{(1)}, \beta_m^{(2)}$, and $Z_m^{(2)}$ are all known quantities in equations (2.4.1) through (2.4.6), and the only unknowns are from the sample area ($\vec{e}_m^{(s)}, \vec{h}_m^{(s)}, \beta_m^{(s)}, Z_m^{(s)}$) because $\bar{\bar{\varepsilon}}, \bar{\bar{\mu}}$ are unknown. Note that $A_m^-, B_m^-, B_m^+, C_m^+$ will also be unknown, but are a direct result of the junction at the sample region. These values can be measured using the actual system, or simulated using the FEM software, and then used to extract information about the material in the sample region.

# CHAPTER 3

# METHODOLOGY

## 3.1. Proposed Study

This thesis investigates a method to model *S*-parameters from the rectangular to square transition waveguide (RTST guide). The approach is based on full-wave FEM modeling and simulation of the waveguide measurement system in Figure 2. The challenge is the size of the numerical problem. The approach here is to numerically determine the *S*-parameters for the transition section so that they can be used to directly excite the sample region. This approach would greatly reduce the computational cost because only the sample region would require simulation. However, additional challenges are to de-embed *S*-parameters of the waveguide test fixture to the sample because the transition guide is not symmetrical, nor does it have a closed form solution. If determined, the de-embedded parameters can then be used to support comprehensive study of different materials in the sample region of the test fixture. Of primary interest is the machined biaxial material proposed by Knisely and Havrilla [1],[7].

## 3.2. Chapter Overview

This chapter is organized as follows. Section 3.3 establishes the FEM requirements to accurately simulate the *S*-parameter matrix for $TE_{mn}$ modes in the RTST guide. Using a WR-90 waveguide divided into multiple segments (Figure 7), Section 3.4 presents and

validates the *T*-matrix analysis to reduce the modeling requirements. Then, Chapter 4 will present analysis and modeling and simulation results of the air-filled RTST test fixture.

In summary, the approach to reduce the computational cost of simulating the complete RTST test fixture follows four steps:

1. Verify the meshing requirements for the FEM model to accurately represent the exact solution found via microwave theory (MT) analysis.
2. Calculate the full *S*-parameter matrix and propagation constants for each segment of the text fixture except for the test sample region.
3. Determine the *T*-parameters for the excitation and transmission waveguide segments.
4. Compare the fields at the sample-guide interfaces as computed by 1) the full-wave simulation and 2) the *T* matrix.
5. Determine the cost savings of the *T*-matrix.

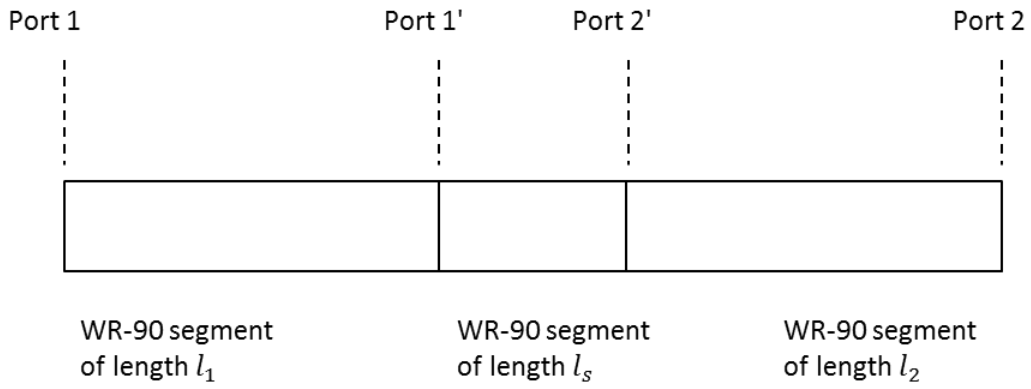


Figure 7. WR-90 waveguide verification test fixture.

### 3.3. Meshing requirements of FEM

To de-embed S-parameters from Port 1 to Port 1′ of Figure 7, a few steps must be taken. First, a validation of the FEM numerical solution to that of the exact solution must be met for the specific mesh used in solving the bounded waveguide problem. The WR-90 verification test fixture in Figure 7 has a theoretical solution and is an ideal test case. As the guide is air-filled, and has no geometrical discontinuities, it represents an ideal lossless transmission line segment. This ideal segment has the S-matrix representation of

$$\bar{S} = \begin{bmatrix} 0 & e^{-\gamma l} \\ e^{-\gamma l} & 0 \end{bmatrix} \tag{3.3.1}$$

$$\gamma = \alpha + j\beta \tag{3.3.2}$$

where $\gamma$ is the complex propagation constant of the line and $l$ is the length of the transmission line segment. Because waves below cut-off will become evanescent and

decay exponentially fast with line attenuation, $\alpha$, the *S*-matrix only represents traveling waves as

$$\bar{S} = \begin{bmatrix} 0 & e^{-j\beta l} \\ e^{-j\beta l} & 0 \end{bmatrix} \tag{3.3.3}$$

To verify the approach, the *S*-matrix of the theoretical solution will be compared to the FEM solution as computed using COMSOL Multiphysics software [8].

### 3.3.1 WR-90 Segment Analysis

The numerical analysis applied by the FEM model is based upon a "mesh" superimposed on the waveguide geometry model. This work uses the FEM solution from COMSOL Multiphysics [8]. The mesh establishes a basis for the linear matrix solution to the fields inside the waveguide and is scaled by the wavelength under study. The mesh of a WR-90 section of waveguide can be seen in Figure 8 where the mesh density is set so that each edge of an element is approximately one-tenth of a wavelength ($\lambda/10$).

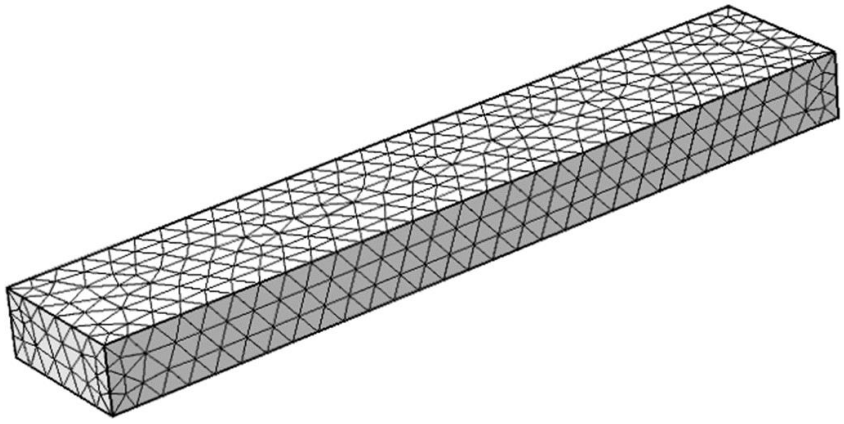

Figure 8. WR-90 segment with $\frac{\lambda}{10}$ trihedral mesh

As the RTST test fixture undergoes an X-band (8.2 to 12.4 GHz) frequency sweep, the mesh size used within the guide should vary (from electrically large to small) as the sweep increases. However, this approach would be impractical as it would require the numerical solution to adapt the mesh to each frequency value. Instead, the center frequency of the X-band sweep is used to define the mesh, and the same mesh is used for all simulations in the sweep. Note that the cut-off frequency for WR-90 is 6.56 GHz [4]. Because of the mesh, the numerical solution will have some error when compared to the exact solution. This error exists because the mesh is fixed and does not change with frequency. The error is analyzed later in this section.

From [4], the propagation constant ($\beta_z$), cut-off frequency ($f_c$), and guided wavelength ($\lambda_g$) for an air-filled WR-90 waveguide are

$$\beta_z(f) = \pm\beta\sqrt{1-\left(\frac{f_c}{f}\right)^2} \quad \text{for} \begin{cases}\beta > \beta_c \\ f > f_c\end{cases} \tag{3.3.4}$$

$$\beta = 2\pi f\sqrt{\varepsilon_o\mu_o} = \frac{2\pi f}{v_p} \tag{3.3.5}$$

$$f_c = \frac{1}{2a\sqrt{\varepsilon_o\mu_o}} \tag{3.3.6}$$

$$\lambda_g = \frac{\lambda_o}{\sqrt{1-\left(\frac{f_c}{f}\right)^2}} \tag{3.3.7}$$

where $\beta_z(f)$ is the propagation constant in the $\hat{z}$ direction. We define the $\hat{z}$-axis as the longitudinal axis of the guide. The cut off frequency represents the lowest fundamental mode which can propagate within the guide, and is solved for $f_c$ = 6.557GHz. Any frequency below this threshold will not be supported by the WR-90 segment. The guide is constructed of perfectly electrically conducting (PEC) material, which forces $\mathrm{TE}_{n0}$ fields on the boundaries to be zero. Because of these boundary conditions, each frequency propagates with a different spatial dependence within the guide. The mesh essentially represents the discretization of the integro-differential operators and is the primary source of computational error when using commercial software such as COMSOL. As long as the relative numerical error is on the order of $10^{-3}$ to $10^{-4}$, the error is considered sufficiently small and acceptable for the de-embedding process [7].

Figure 9 shows the results of the FEM-based computation of the WR-90 *S* parameters. The error is shown in Figure 10 and verifies the quality of the mesh. It is important to note that the test case results in an ideal symmetric *S*-matrix. Therefore, only the $S_{11}$ and $S_{21}$ values are shown in Figure 9 and only $S_{12}$ and $S_{21}$ errors are shown in Figure 10.

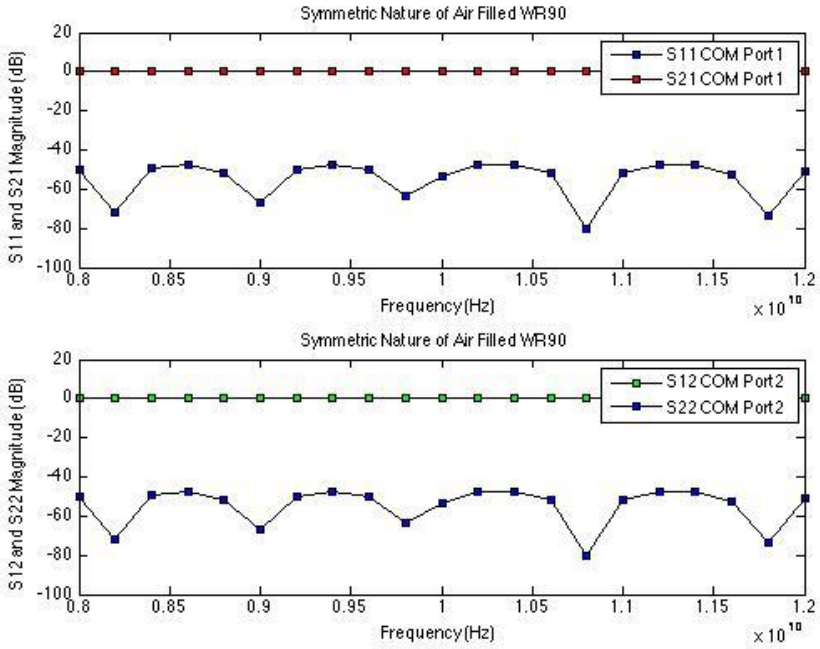


Figure 9. *S* parameters for air-filled WR-90.

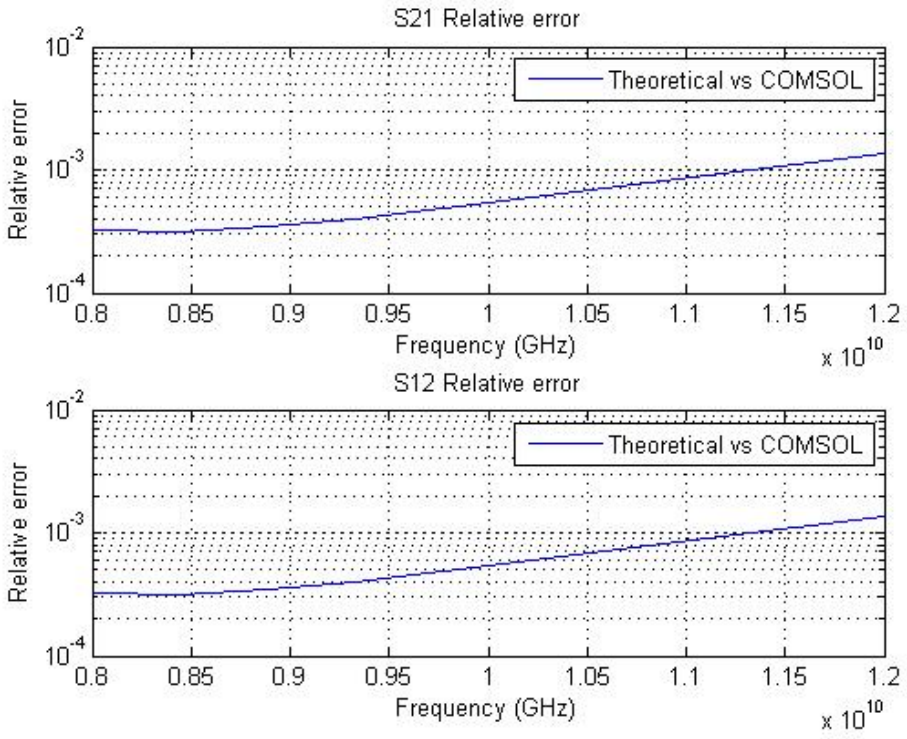


Figure 10. Relative error of theory versus numerical solution (COMSOL).

As seen in Figure 9 and Figure 10, the symmetric nature of the guide exhibits reciprocal *S*-parameters, i.e. $S_{12} = S_{21}$ and $S_{11} = S_{22}$. Also, the meshing size for the WR-90 has small relative error when comparing the numerical solution to that of equation (3.3.3).

### 3.3.2 Square Sample Region Analysis

Similarly to the WR-90 section, the square cross-sectional waveguide section of the RTST which holds the sample is simulated. This square waveguide has dimensions of $a_1 \times a_1$ where $a_1$ is the width of the WR-90 guide. The change in dimension dictates a new propagation constant and cutoff frequency per mode for the square region as [3]

$$f_{c_{mn}} = \frac{1}{2\pi\sqrt{\mu\varepsilon}}\sqrt{\left(\frac{m\pi}{a_1}\right)^2 + \left(\frac{n\pi}{a_1}\right)^2} \tag{3.3.8}$$

$$\beta(z)_{mn} = \left(2\pi f\sqrt{\mu\varepsilon}\right)\sqrt{1 - \left(\frac{f_{c_{mn}}}{f}\right)^2} \tag{3.3.9}$$

where $f_{c_{mn}}$ is the cut off frequency per mode and $\beta(z)_{mn}$ is the propagation constant within the square guide. If we model the square guide as air filled, its scattering matrix should match (3.3.3) as an ideal lossless transmission line. The *S* parameters and error between the numerical solution and the theoretical values are shown in Figure 11.

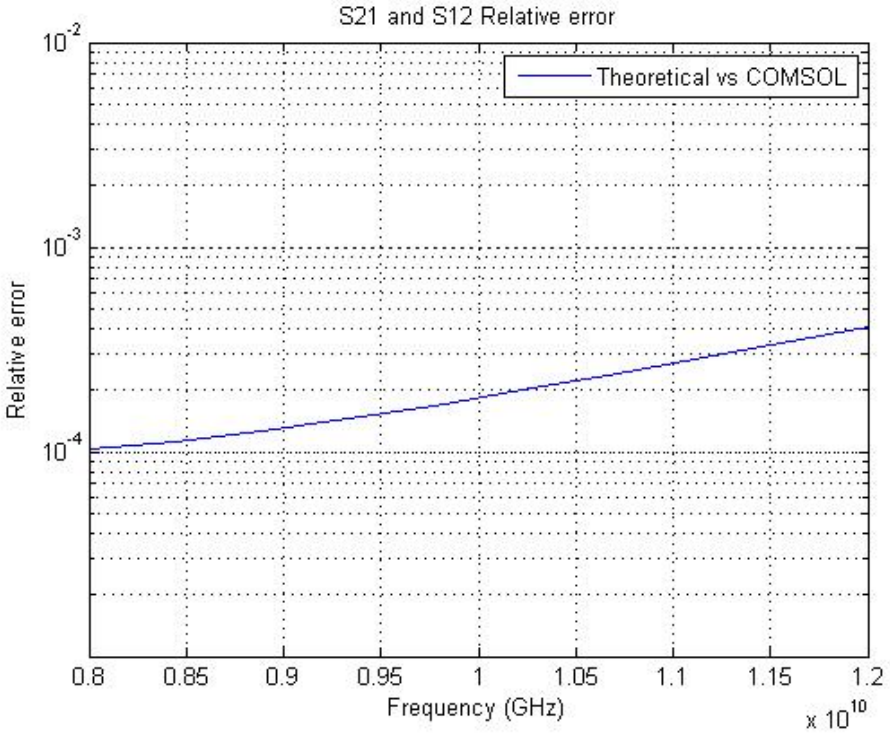


Figure 11. Relative error of square cross-sectional waveguide simulation.

Due to the reciprocal nature of the square waveguide, $S_{21}$ and $S_{12}$ have the same relative error. It has been shown that the numerical solution is valid for both the WR-90 and square cross-section segments of the RTST guide. Using the analysis from this section, coupled with full wave simulations of the entire RTST fixture, one should be able to uniquely characterize the tapered section through an iterative approach using higher order mode analysis along with *T*-matrix theory. Hence, full-wave simulation of the entire RTST test fixture can be a baseline for comparison between the numerical solution and the de-embedding process, represented by the calibration process in the measurement system.

### 3.4. De-embedding and *T*-Matrix Validation

Section 3.3 showed that the FEM numerical solution can be computed using a single mesh for the complete frequency sweep even though the WR-90 and square cross-sectional waveguide segments have differently sized domains. Later, the de-embed process will be applied from each of these two segments to determine the *S* parameters at the sample face. However, the simulation requires a finite-length excitation segment and transmission segment as shown in Figure 12. In a measurement system, the calibration process is performed at the desired plane of reference. The simulation requires the simulation of a finite-section of WR-90 guide (segments 1 and 5) that precede the

transition segments (segments 2 and 4). Therefore, the de-embed process must be applied when comparing mode-matching models or measurement to simulation.

To demonstrate the de-embed process, a simplified all-WR-90 test fixture is studied first (shown in Figure 12).

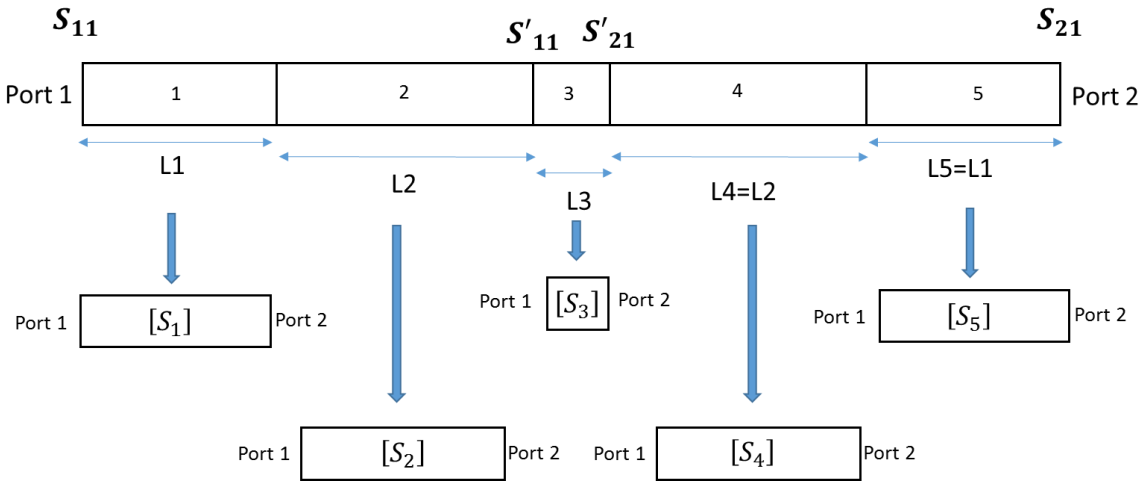


Figure 12. All-WR-90 test fixture.

Each individual section is characterized by a two-port *S*-matrix $\bar{S}_n$. The reciprocal nature of the air filled guide means that each section will have the same *S*-parameter values shown in Figure 9.

Referring back to equation (3.3.3), only $S_{21}$ and $S_{12}$ have non-zero values. Therefore, only the errors for $S_{21}$ and $S'_{21}$ are considered. Also, the reciprocal nature of the WR-90 guide results in $S_{21} = S_{12}$, and it is unnecessary to de-embed Port 1 to Port 1′ to solve for $S'_{12}$.

The solution for $S_{21}$ at the de-embed location ($S'_{21}$) uses the length $l = L1 + L2$ as

$$S'_{21} = S_{21} e^{+j2\pi\beta l} \tag{3.4.1}$$

Although some software tools may allow the user to define a new reference plane at any location within the guide, COMSOL only allows the port to be defined at the outer most boundary which would be similar to an actual measurement. Also, based on the defined coordinate system used to calculate the *S* parameter, it may be necessary to multiply by $-1$. By properly applying the de-embed technique, the analytic and numerical solutions for $S'_{21}$ can be compared at arbitrary reference planes within the guide.

To demonstrate the above, the complex *S* parameters at Port 2 and the relative error are shown in Figure 13 and Figure 14. Likewise, the *S* parameters at Port 2′ and the relative error are shown in Figure 15 and Figure 16. In each case, the error is on the order of 0.001.

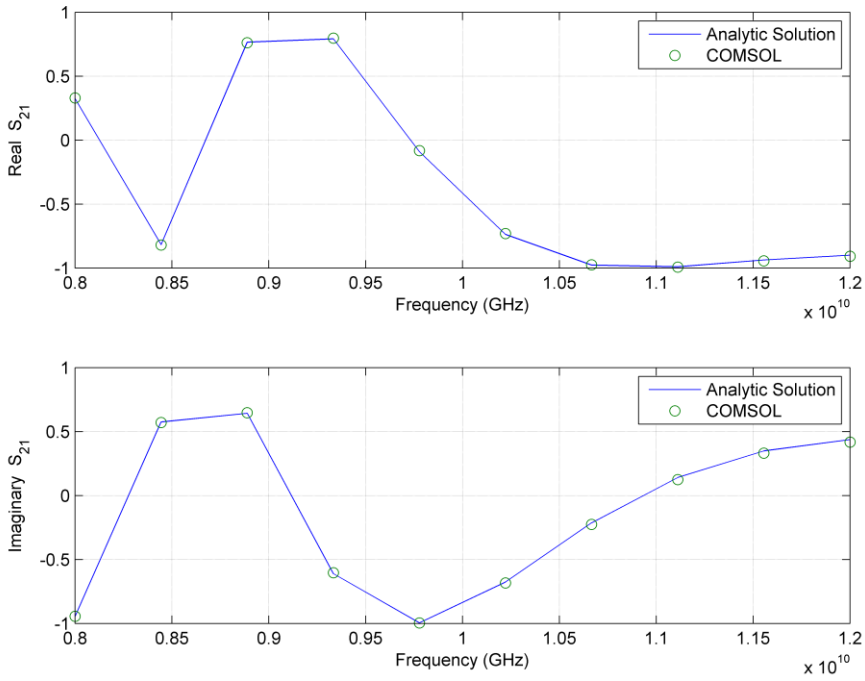


Figure 13. $S_{21}$ at Port 2 for All-WR-90 guide.

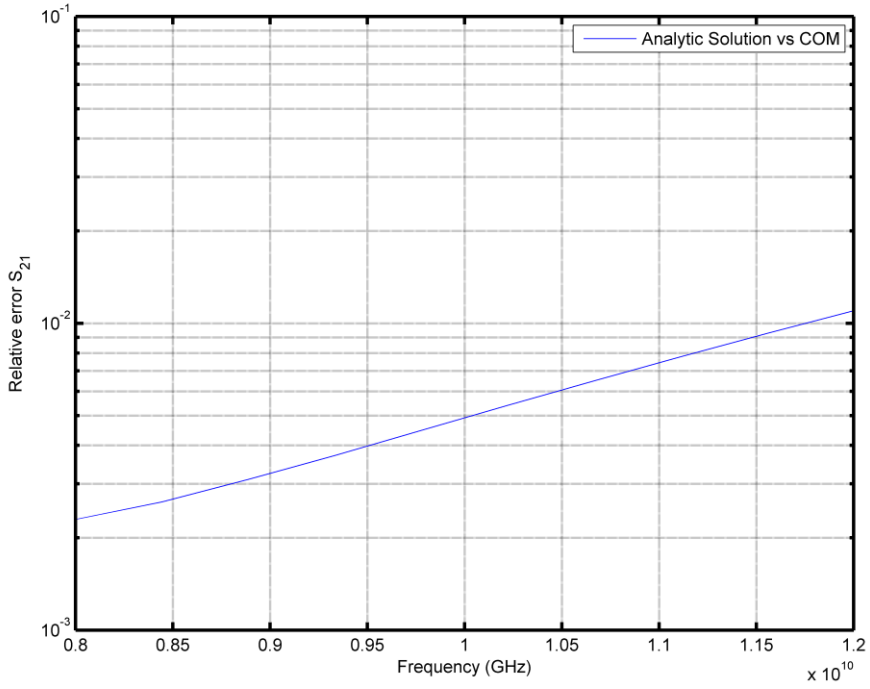


Figure 14. Relative error of $S_{21}$ at Port 2.

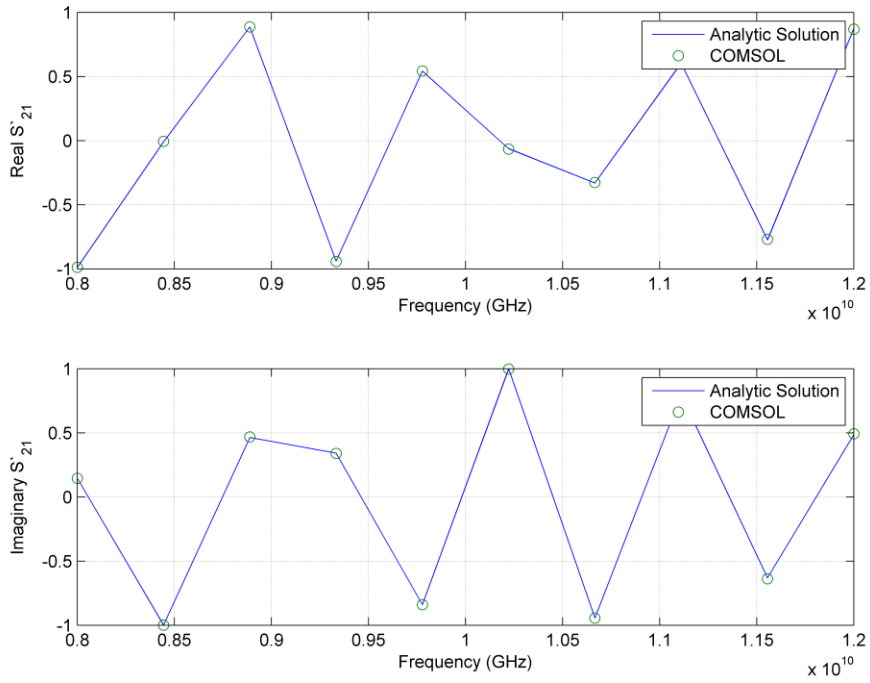


Figure 15. $S'_{21}$ at new reference plane for All-WR90 guide.

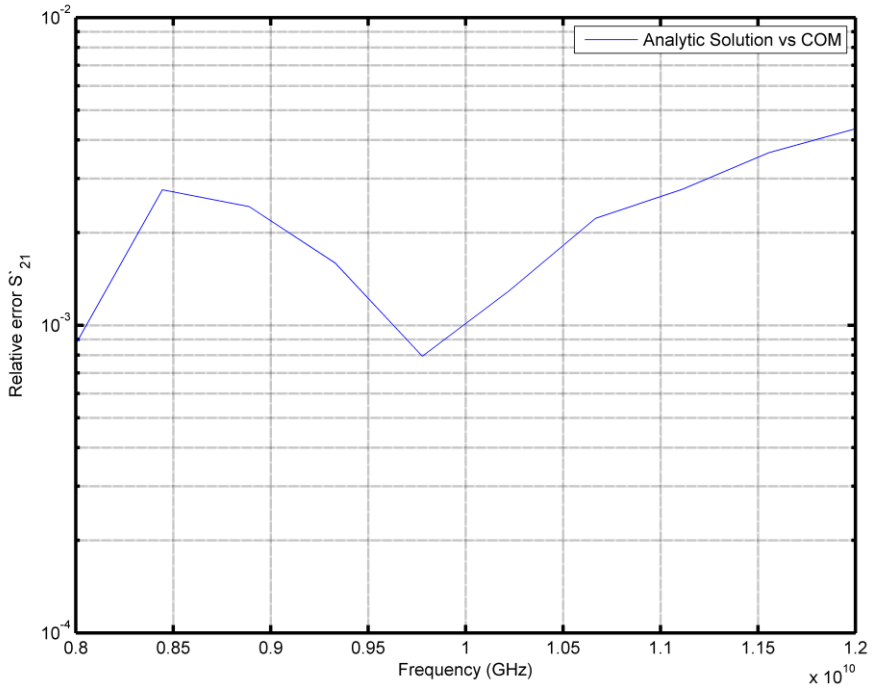


Figure 16. Relative error of $S'_{21}$ at new reference plane.

The relative error following the de-embed process has the same order of magnitude as the mesh error. In other words, we are able to define a new reference plane at any location within the guide.

### 3.4.1 Propagation Constant

The de-embed process utilizes the propagation constant $\beta$, solved per frequency value within COMSOL's numerical solution. The relative error between the numerical value of the propagation constant is shown in Figure 17. It is easy to see that the numerical solution agrees with the theoretical solution for $\beta$ very well.

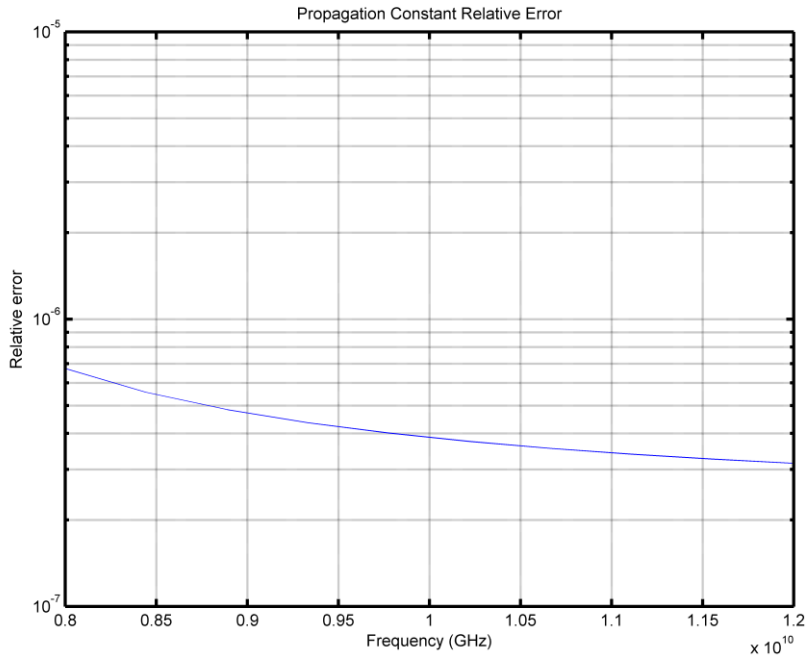


Figure 17. Relative error of propagation constant in WR-90 waveguide.

### 3.4.2 *T*-Matrix Validation

As seen in Figure 12, each individual waveguide segment is analyzed separately and yields its own scattering matrix $[S_n]$. Following equations (2.3.2) through (2.3.5), one is able to convert each segment into its corresponding *T*-Matrix, and then cascade them together using equation (2.3.6) as represented in Figure 18.

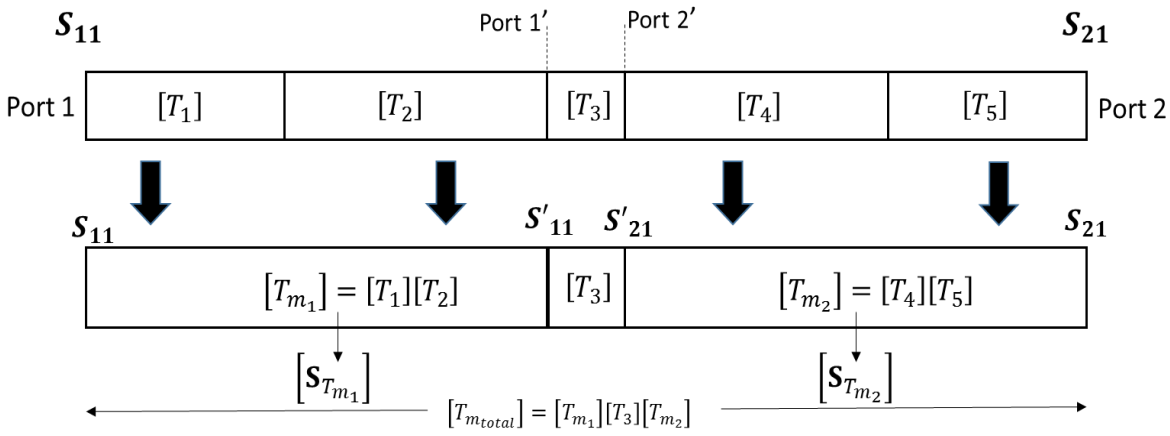


Figure 18. *T*-Matrix conversion of All-WR90 guide.

Once the cascade is applied, equations (2.3.8) through (2.3.11) are used to convert the overall *T*-matrix $[T_{mtotal}]$ matrix back into *S*-parameters for the entire-cascaded network.

The fields induced at Port 1 can be propagated to the sample using the *T*-matrices. Then, the fields at the primed reference planes may be used to excite the sample without direct simulation of the fields in the transition section of the guide. Thus, computing time and memory are reduced. Because the analytic solution for $S_{11}$ is zero, an absolute error will be used. The absolute error for $S_{11}$ is seen in Figure 19 and the relative error for $S_{21}$ is displayed in Figure 20. It is important to note that the *S* parameters used in the "*T*-matrix" solution utilize equations (2.3.7) through (2.3.11) to yield its values, while the analytic solution utilizes equations (3.3.3) through (3.3.6).

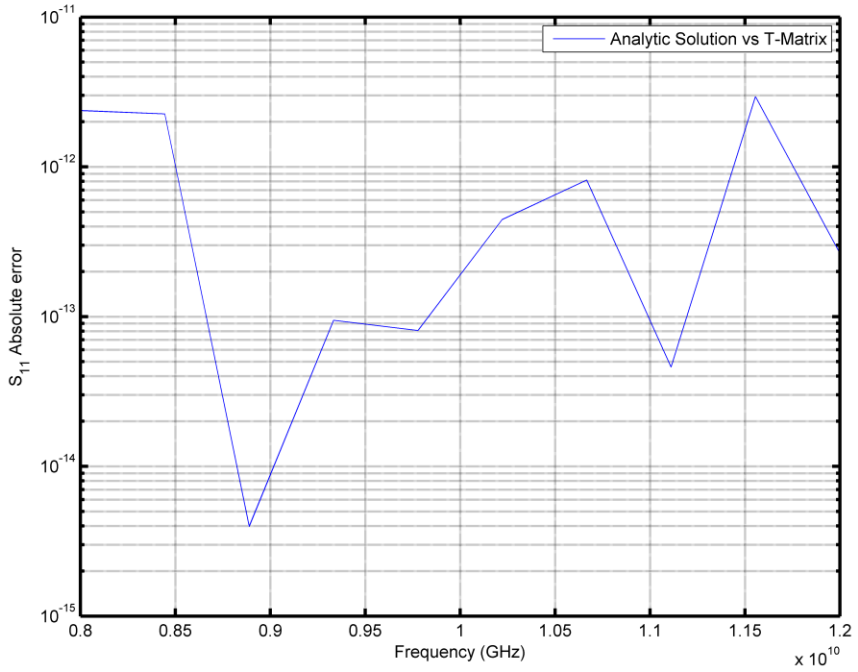


Figure 19. Absolute error of *T*-matrix solution for $S_{11}$ in Figure 18.

The analytic solution utilizes the length $l = 2l_1 + 2l_2 + l_3$ to solve for the fields located at Port 2.

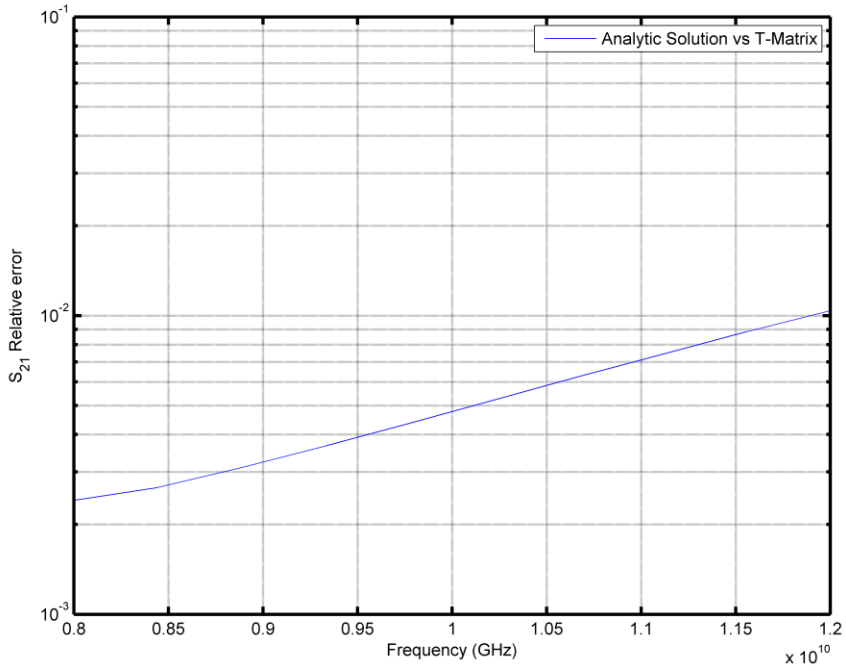


Figure 20. Relative error of *T*-matrix solution for $S_{21}$ in Figure 18.

To solve for the incoming and outgoing wave at any arbitrary reference plane, the corresponding cascaded *T*-matrix must equate all previous regions for which the wave has propagated through. This cascade is mathematically defined as left-to-right [6]. Therefore, for a new reference plane at location $S'_{21}$, the cascaded *T*-matrix must take the form.

$$T_M = T_1 T_2 T_3 = T_{m_1} T_3 \tag{3.4.3}$$

This cascading will yield the $S_{21}$ value at the exit of the sample region using equation (2.3.10). This value is shown as $S'_{21}$ in Figure 18. Comparing this value with the analytic

solution obtained by equations (3.3.3) through (3.3.6) with $l = l_1 + l_2 + l_3$ is shown in Figure 18.

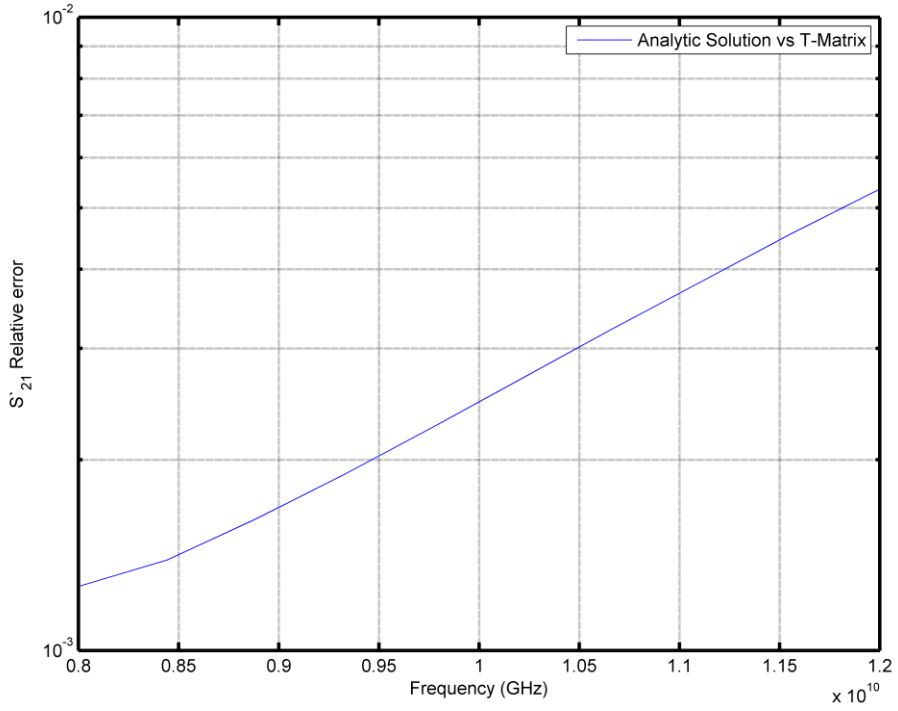


Figure 21. Relative error of *T*-matrix solution for$S'_{21}$ in Figure 18.

It is clear by analysis that that the *T*-matrix is a valid way to solve for the net response of individual waveguide sections. It and the de-embed process of (3.4.1) are valid approaches for the all-WR90, air filled, passive structure. This analysis will be carried over to the RTST structure next.

### 3.5. Taper Characterization

The WR-90 and square waveguide sections were easy to analyze since a theoretical solution was available for the scattering parameters. The tapered transition, however, will be more difficult as there is no analytic solution available to compare against. Without a analytic solution, we cannot validate the numerical solution for the taper without a full analysis. This will include exploring higher order modes induced within the tapered transition, along with looking at the complex electric and magnetic fields at various regions within the taper.

If we were to look down the $\hat{z}$ axis of the guide, as seen in Figure 19, there is a large discontinuity at the plane between the WR-90 and the square sample region.

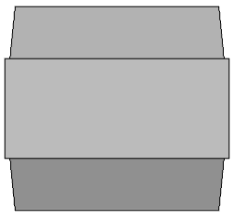

Figure 22. Perspective view along longitudinal axis of RTST guide.

The discontinuity will excite higher-order $\mathrm{TE}_{mn}$ modes within the taper, and must be accounted for to properly de-embed the data to a new reference plane. This reference

plane will then be used to excite the sample region, thus reducing the computation time of the numerical model.

### 3.5.1 Total fields in tapered waveguide.

The *S* parameters represent a collection of the modal amplitudes measured at a port (both forward and backward traveling waves). For an excitation in segment 1 ($\vec{E}_0^{(1)}$), the parameters $S_{11}$ and $S_{21}$ are

$$S_{11}(z_0, f) = \frac{\int \left( \vec{E}^{(1)}(x, y, z_0; f) - \vec{E}_0^{(1)}(x, y, z_0; f) \right) \cdot \vec{E}_0^{(1)*}(x, y, z_0; f) \mathrm{d}x\mathrm{d}y}{\int \vec{E}_0^{(1)}(x, y, z_0; f) \cdot \vec{E}_0^{(1)*}(x, y, z_0; f) \mathrm{d}x\mathrm{d}y} \tag{3.5.1}$$

$$S_{21}(z_3, f) = \frac{\int \vec{E}^{(2)}(x, y, z_3; f) \cdot \vec{E}_0^{(2)*}(x, y, z_3; f) \mathrm{d}x\mathrm{d}y}{\int \vec{E}_0^{(2)}(x, y, z_3; f) \cdot \vec{E}_0^{(2)*}(x, y, z_3; f) \mathrm{d}x\mathrm{d}y} \tag{3.5.2}$$

where $\vec{E}^{(1)}$ and $\vec{E}^{(2)}$ are the total fields in segments 1 and 2 and $\vec{E}_0^{(1)}$ and $\vec{E}_0^{(2)}$ are the waves entering Port 1 and leaving Port 2, respectively. The asterisk denotes complex conjugation. In Equations (3.5.1) and (3.5.2), the reference planes are specified at the $z = z_0$ plane for Port 1 and $z = z_3$ for Port 2. For dominant-mode excitation at Port 1, and sufficiently long waveguide segments, $\vec{E}_0^{(1)}$ and $\vec{E}_0^{(2)}$ are $TE_{10}$.

However, when a complicated junction exists such as that presented by an anisotropically filled region, and when the segment is not sufficiently long, then the total field measurement includes higher-order modes that have not sufficiently decayed. In these

cases, modal expansion of the fields as in Section 2.4 is needed to analyze the *S* parameters.

### 3.5.2 Higher-order modes in tapered waveguide

The $\vec{E}_0^{(1)}$ term represents the dominant $TE_{10}$ mode across the Port 1 surface ($d\Omega$), and $\vec{E}^{(1)} = \Sigma_m \vec{E}_m^{(1)}$ term represents the fields caused by all *M* modes. As higher-order modes will affect the scattering parameters, we investigate how many modes are excited by the test fixture. Also, the taper grows from a rectangular WR-90 to a square waveguide, so, it is safe to assume that the taper will support just as many modes as a square waveguide would. According to [9], the estimated number of modes supported within a square waveguide structure is

$$N_{square} = 1.5711 \left(\frac{2af}{c}\right)^2 \tag{3.5.3}$$

where $c$ is the speed of light, $a$ is the width of the square region, and $f$ is the frequency of the incident wave. This equation was found by numerically computing the total number of TE and TM modes in a square waveguide as a function of normalized frequency for the first 1000 modes. A regression analysis was then carried out to find the best second order polynomial fit, and then coefficients were obtained by using maximum likelihood estimates [9]. The highest number of supported modes will be caused by the upper frequency in the X-band sweep ($f = 12$ GHz) yielding the value of $N_{square} = 5.2$. Therefore, we will analyze the taper for the lowest ordered 6 modes. For any excitation

frequency, only the modes whose cut-off frequency falls below the X-band sweep will be excited within the taper. In other words, $f_{c_{square}} < f$ for the mode to propagate within the guide. Recalling equation (3.3.8), one is able to solve for the cut off frequency per mode number as displayed in Table 1.

Table 1. Cut-off Frequency per mode number.

| M | n | Cut off Frequency $\boldsymbol{f_c}$ |
|---|---|---|
| 1 | 0 | 6.557 GHz |
| 0 | 1 | 6.557 GHz |
| 1 | 1 | 9.273 GHz |
| 2 | 0 | 13.114 GHz |
| 0 | 2 | 13.114 GHz |
| 1 | 2 | 14.662 GHz |
| 2 | 1 | 14.662 GHz |
| 3 | 0 | 19.671 GHz |
| 5 | 0 | 32.786 GHz |
| 7 | 0 | 45.9 GHz |

Under the X-band sweep, there will be multiple modes supported by the taper. The strongest response is expected to be seen by the dominant $TE_{10}$ mode, but $TE_{11}$ will also contribute. This behavior can be seen in the normalized magnitude graphs exported from COMSOL (Figure 23 to Figure 27). Red indicates strong field magnitude and blue indicates very weak magnitude.

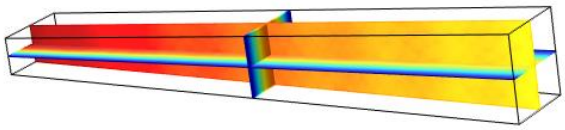

Figure 23. Dominant $TE_{10}$ mode within taper

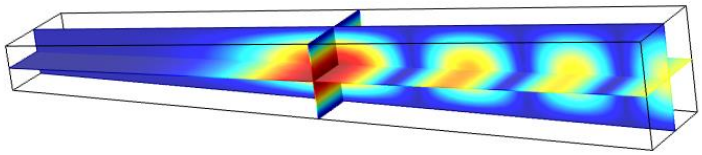

Figure 24.Response from $TE_{01}$ mode excitation

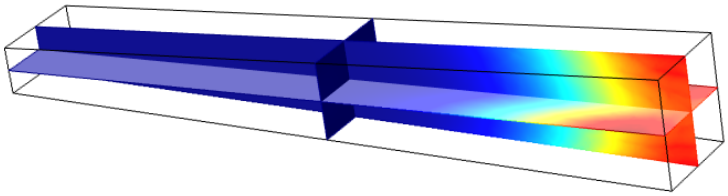

Figure 25. Response from $TE_{11}$ mode excitation

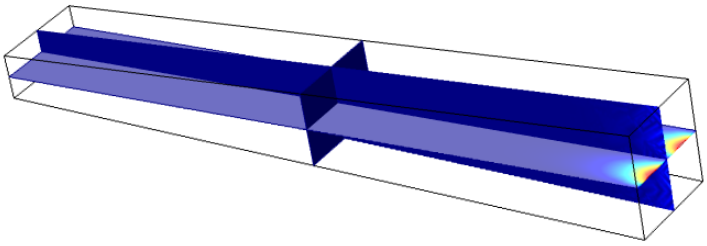

Figure 26. Response from $TE_{20}$ mode excitation

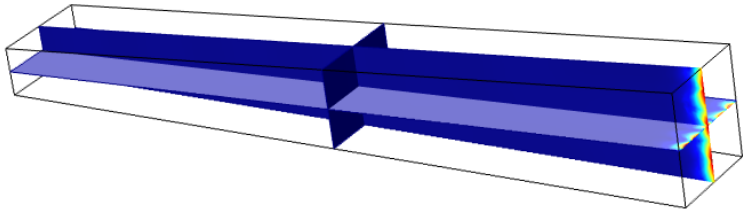

Figure 27. Response from $TE_{50}$ mode excitation

It is clear that other modes exist within the taper, since theses modes have non-zero electric and magnetic field amplitudes. Even though these modes evanesce, the question remains: "Are we able to model the taper as a lossless transmission line if it is air filled?" If the taper is proven to be a lossless transmission line, then equation (3.3.3) may be utilized to model the scattering parameters of the taper, and then serve as a baseline for the numerical solution relative error analysis.

For a transmission line segment to be considered lossless, it must meet five criteria

$$|S_{11}|^2 + |S_{21}|^2 = 1 \tag{3.5.4}$$

$$|S_{12}|^2 + |S_{22}|^2 = 1 \tag{3.5.5}$$

$$S_{11}^* S_{12} + S_{21}^* S_{22} = 0 \tag{3.5.6}$$

$$|S_{11}||S_{12}| = |S_{21}||S_{22}| \tag{3.5.7}$$

$$-\arg(S_{11}) + \arg(S_{12}) = -\arg(S_{21}) + \arg(S_{22}) + \pi \tag{3.5.8}$$

$$\arg(x) = \operatorname{atan}\left(\frac{\operatorname{Im}(x)}{\operatorname{Re}(x)}\right) \tag{3.5.9}$$

These criteria for a lossless network come from the unitary condition: $S^H S = I$ where $I$ is the identity matrix and the superscript $H$ is the Hermitian Transpose (transposed complex conjugate). But as there are multiple modes present within the taper, the *S*-parameter criteria for a lossless guide, Equations (3.5.4) through (3.5.8), must be satisfied for each mode and excitation frequency.

To study the modes, the excitation of the taper is swept through different $TE_{mn}$ modes. Then, the *S* parameters are analyzed per mode. According to [1], the taper is designed to support only $TE_{m0}$ modes, where *m* is an odd integer. This claim is investigated using the modes listed in Table 1which lists other modes and their corresponding cutoff frequencies. Specific interest lies in the $TE_{11}$ mode, which has a cutoff frequency equal to: $f_{c_{11}} = 9.273$ GHz. This value is below half the frequencies used in the X-band excitation and means that the $TE_{11}$ is able propagate within a square dimension for the upper half of the X-band sweep (10 GHz to 12 GHz). Therefore, the taper is excited by $TE_{mn}$ modes: $TE_{10}$, $TE_{01}$, $TE_{11}$, $TE_{20}$, $TE_{30}$, $TE_{50}$, and $TE_{70}$.

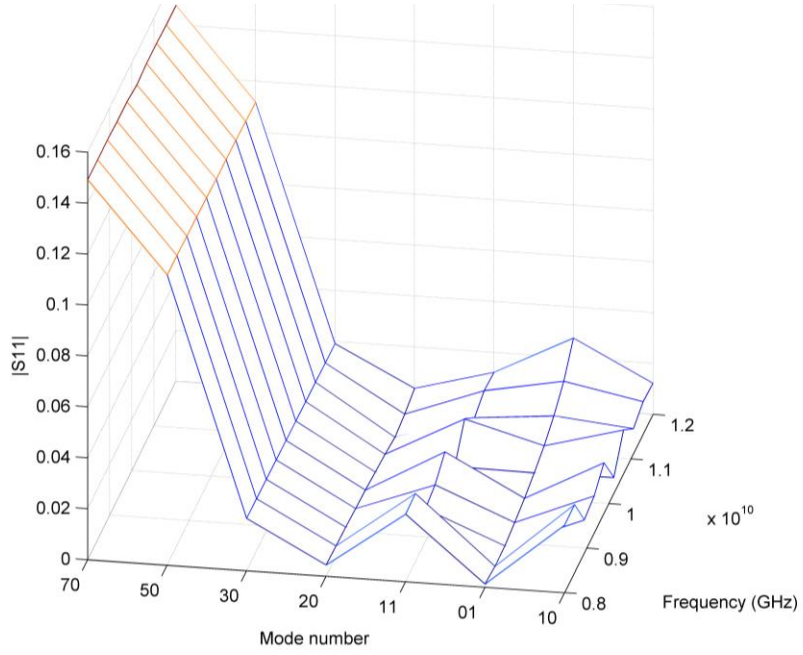


Figure 28. $S_{11}$ magnitude of transition waveguide by mode and frequency.

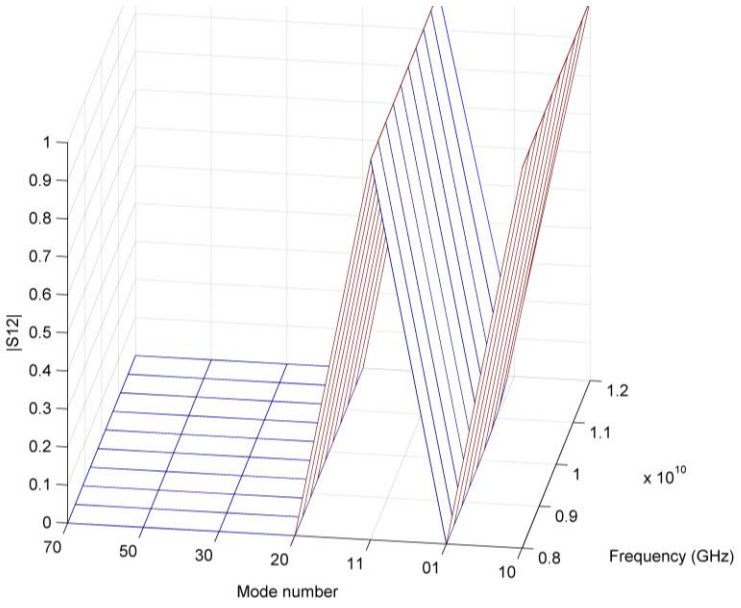


Figure 29. $S_{12}$ magnitude of transition waveguide by mode and frequency.

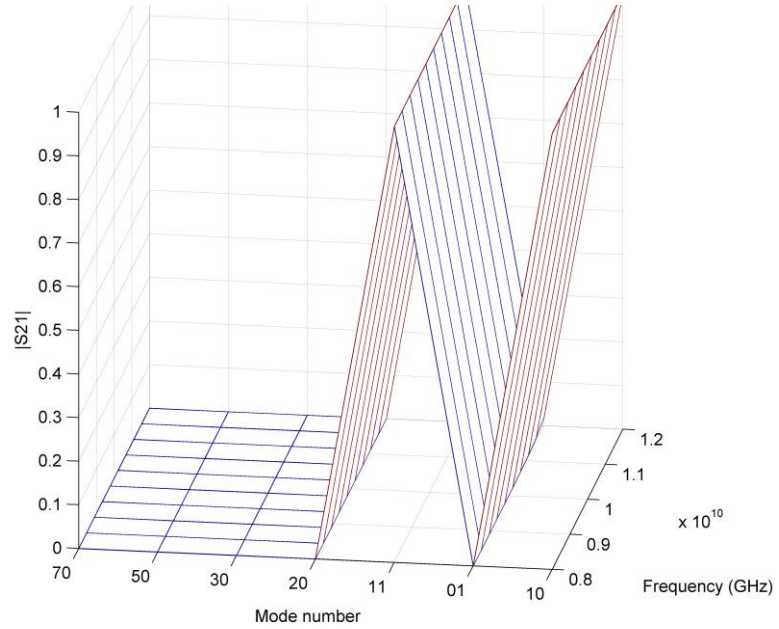


Figure 30. $S_{21}$ magnitude of transition guide by mode and frequency.

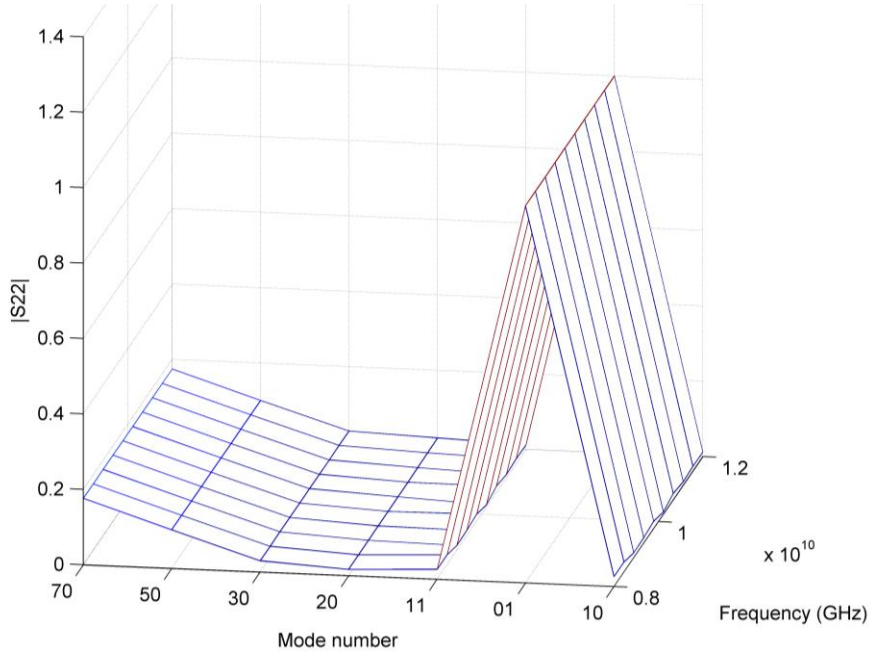


Figure 31. $S_{22}$ magnitude of transition guide by mode and frequency.

Figure 29 and Figure 30 make the taper seem reciprocal in nature as $S_{12} = S_{21}$. These figures also show ideal propagation through the guide for modes $TE_{10}$ and $TE_{11}$. By visual analysis, a few intuitive things can be taken away from Figure 28 to Figure 31. As the taper gradually changes from rectangular to square, the square region supports modes which the rectangular does not. This can be seen for the $S_{22}$ values measured at Port 2 and thus within the square region. The high-order modes $TE_{30}$, $TE_{50}$, and $TE_{70}$ all yield non-zero reflection as compared to the dominant $TE_{10}$ mode at Port 2. Also, the $S_{21}$ and $S_{12}$ values show ideal transmission line behavior for $TE_{10}$ and $TE_{11}$ modes within the guide. Therefore, using Equations (3.5.3) through (3.5.8), the taper may be modeled as a lossless transmission line.

The lossless transmission line criteria are graphed for the $TE_{10}$ and $TE_{11}$ modes in Figure 32 to Figure 39. The results show that the dominant mode and first high-order mode within the taper can be represented as an ideal lossless transmission line.

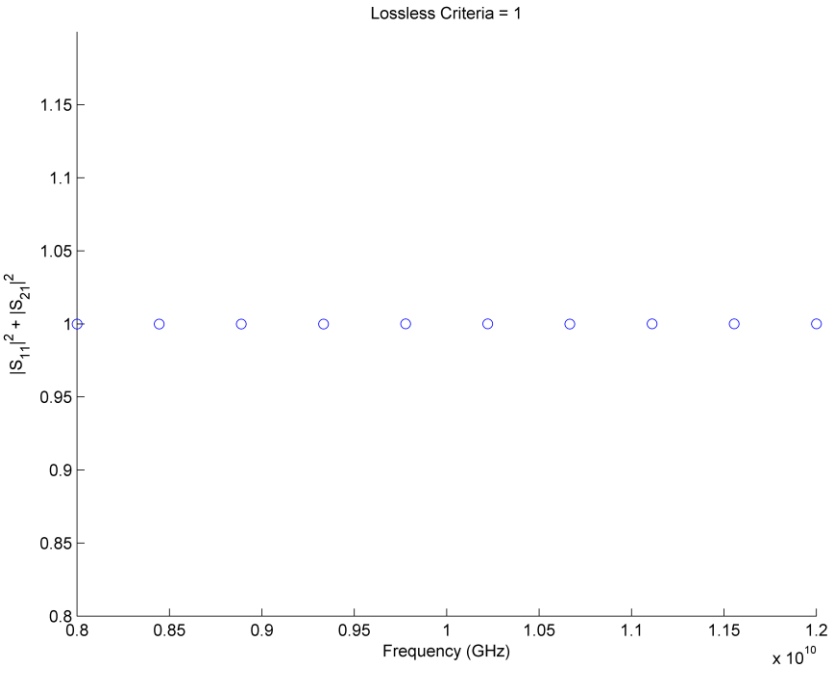


Figure 32. Equation (3.5.4) solved for $TE_{10}$ mode within transition guide.

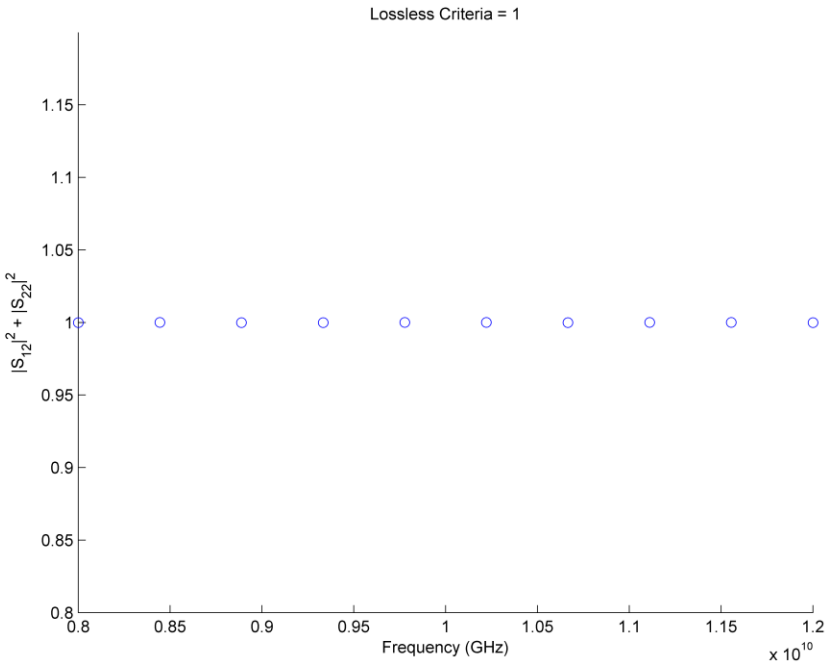


Figure 33. Equation (3.5.5) solved for $TE_{10}$ mode within transition guide.

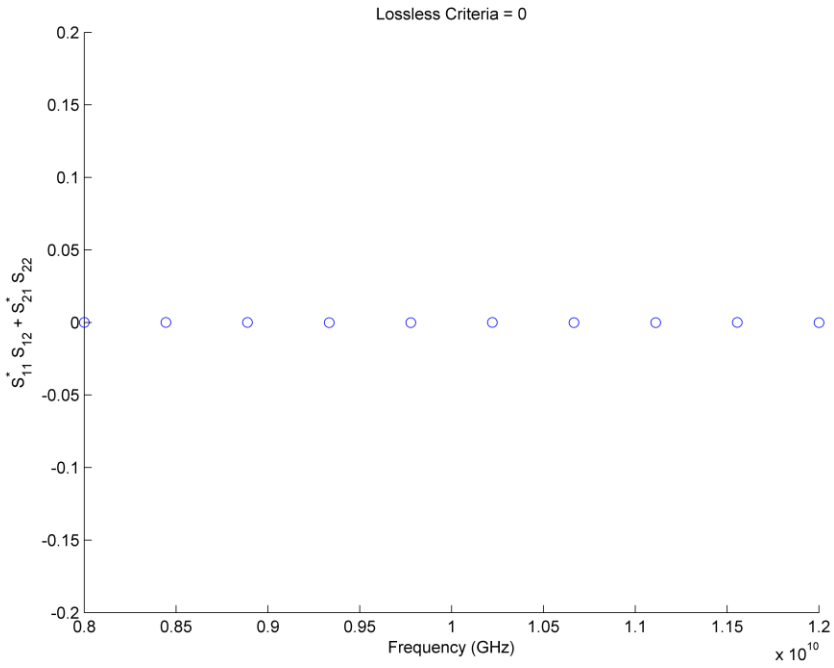


Figure 34. Equation (3.5.6) solved for $TE_{10}$ mode within transition guide.

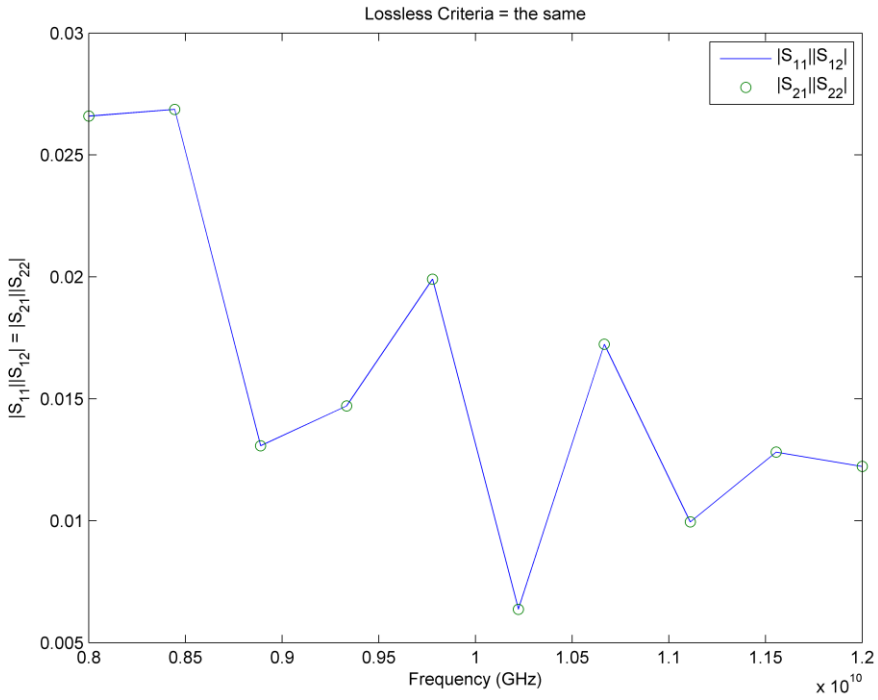


Figure 35. Equation (3.5.7) solved for $TE_{10}$ mode within transition guide.

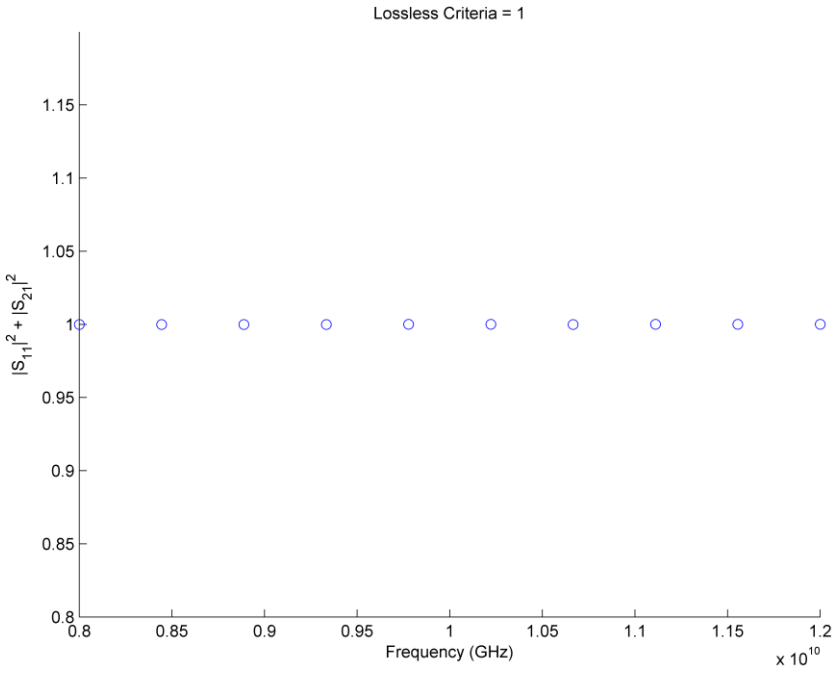


Figure 36. Equation (3.5.4) solved for $TE_{11}$ mode within transition guide.

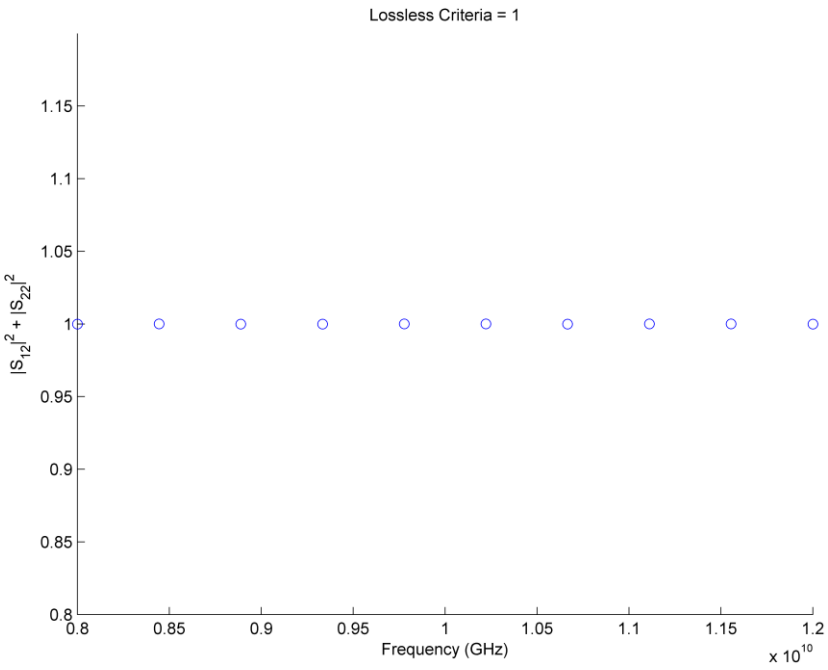


Figure 37. Equation (3.5.5) solved for $TE_{11}$ mode within transition guide.

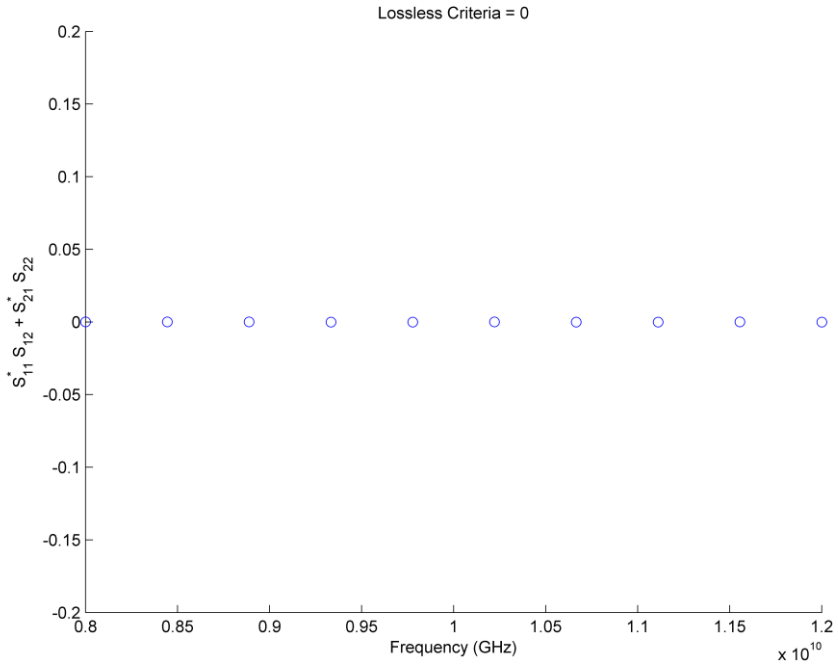


Figure 38. Equation (3.5.6) solved for $TE_{11}$ mode within transition guide.

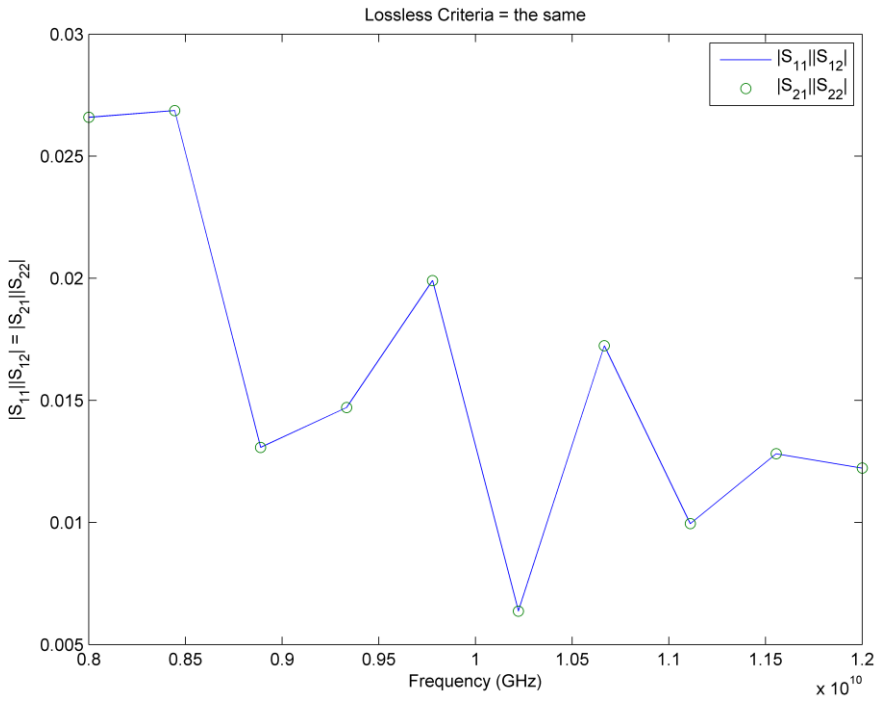


Figure 39. Equation (3.5.7) solved for $TE_{11}$ mode within transition guide.

### 3.6. Summary

When excited by the dominant mode at the WR-90 port of the transition waveguide, high-order modes are excited at Port 1 and Port 2. The scattering parameters show that the air-filled guide only supports TE10 and TE11 modes. To model the waveguide measurement system without explicitly modeling the transition guide, the excitation at the sample region must include both the dominant and first high-order mode. Then, the scattering parameters can be calculated for the sample region with increased efficiency.

# CHAPTER 4

# RESULTS

## 4.1. Experimental Set Up

From Section 3.5, it was shown that the junction between the transition guide and sample waveguide section (Figure 40) causes $TE_{11}$ modes to excite a sample in addition to the $TE_{10}$ mode. Therefore, if the sample region is to be excited directly to reduce the computational cost, then the excitation and calculation of the *S* parameters must be calculated for multi-mode fields.

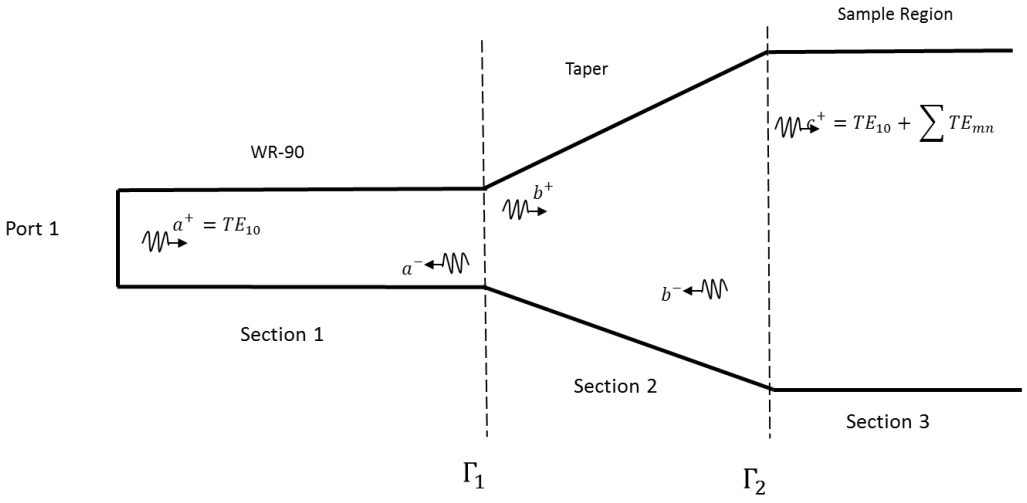


Figure 40. Single-mode excitation of WR-90 waveguide (Section 1) connected to square waveguide (Section 3) using transition waveguide (Section 2). High-order modes are excited at waveguide junctions causing multi-mode propagation at junction to Section 3.

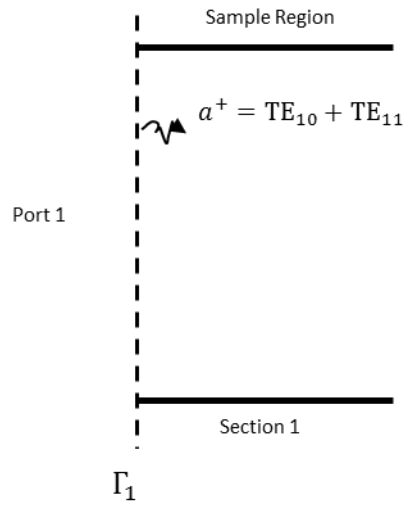


Figure 41. Multi-mode excitation of square waveguide (sample region).

To test the hypothesis, the field patterns at the guide-sample interface ($\Gamma_2$ in Figure 40 and $\Gamma_1$ in Figure 41) are compared. Due to the varying geometry of the transition guide, each section of the overall system must be individually modeled to show the field relationships. The rectangular-to-square waveguide was designed in the collective works of the authors of [1] and was specified to be *y*-invariant for the frequency band. If Port 1 is excited by a $TE_{10}$ mode, then Maxwell's equations separate into two sets of modal equations: $TE_z$ and $TM_z$. However, the $TM_z$ modal equations will yield a trivial solution for biaxial samples and are ignored [2]. Therefore, only the $TE_z$ modes are needed to fully characterize the tapered waveguide for biaxially dielectric samples. Following the discussion on transverse electric waves within bounded PEC structures in [4], we can model the incoming and outgoing waves shown in Figure 40. Also, as Section 1 is air

filled and assumed to be perfectly matched to the excitation port, the only forward going wave will be the excitation field. For a $TE_{10}$ excitation, the forward going waves ($a^+$) are

$$E_y = -\frac{A_{10}^+}{\varepsilon}\frac{\pi}{a}\sin(k_x x)e^{-j\beta_z z} \tag{4.1}$$

$$H_x = A_{10}^+\frac{\beta_z}{\omega\mu\varepsilon}\frac{\pi}{a}\sin(k_x x)e^{-j\beta_z z} \tag{4.2}$$

$$H_z = -j\frac{A_{10}^+}{\omega\mu\varepsilon}\left(\frac{\pi}{a}\right)^2\cos(k_x x)e^{-j\beta_z z} \tag{4.3}$$

where $E_x, E_z$, and $H_y$ all equal zero an. The reflected wave ($a^-$) caused by the junction at the leftmost side of the tapered guide, contains higher order modes. Likewise, the high-order modes are

$$E_x = \sum_{m,n}\frac{k_{y,n}}{\varepsilon}\cos(k_{x,m}x)\sin(k_{y,n}y)\left[A_{mn}^+e^{-j\beta_{z,mn}z} + A_{mn}^-e^{+j\beta_{z,mn}z}\right] \tag{4.4}$$

$$E_y = \sum_{m,n} -\frac{k_{x,m}}{\varepsilon}\cos(k_{y,n}y)\sin(k_{x,m}x)\left[A_{mn}^+e^{-j\beta_{z,mn}z} + A_{mn}^-e^{+j\beta_{z,mn}z}\right] \tag{4.5}$$

$$H_x = \sum_{m,n}\frac{k_{x,m}\beta_z}{\omega\mu\varepsilon}\cos(k_{y,n}y)\sin(k_{x,m}x)\left[A_{mn}^+e^{-j\beta_{z,mn}z} + A_{mn}^-e^{+j\beta_{z,mn}z}\right] \tag{4.6}$$

$$H_y = \sum_{m,n}\frac{k_{y,n}\beta_{z,mn}}{\omega\mu\varepsilon}\cos(k_{x,m}x)\sin(k_{y,n}y)\left[A_{mn}^+e^{-j\beta_{z,mn}z} + A_{mn}^-e^{+j\beta_{z,mn}z}\right] \tag{4.7}$$

$$H_z = \sum_{m,n} -j\frac{k_{c,mn}^2}{\omega\mu\varepsilon}\cos(k_{y,n}y)\cos(k_{x,m}x)\left[A_{mn}^+e^{-j\beta_{z,mn}z} + A_{mn}^-e^{+j\beta_{z,mn}z}\right] \tag{4.8}$$

where

$$k_{c,mn}^2 \equiv \left(\frac{2\pi}{\lambda_{c,mn}}\right)^2 = k^2 - \beta_{z,mn}^2 = k_{x,m}^2 + k_{y,n}^2 = 2\pi f_c\sqrt{\mu\varepsilon} \tag{4.9}$$

$$= \left(\frac{m\pi}{a}\right)^2 + \left(\frac{n\pi}{b}\right)^2$$

$$(\beta_z)_{mn} = k\sqrt{1 - \left(\frac{f_c}{c}\right)^2} \tag{4.10}$$

Equations (4.1) through (4.3) model the incoming wave to the system, where equations (4.4) through (4.10) represent the possible TE field formations located at any transverse region within the guide. It is good to note that Section 3 of Figure 40 will only have forward going waves as the port is assumed to be perfectly matched.

Since the WR-90 and transition regions are air filled, TM$^z$modes are also able to exist. These field configurations are represented by equations (4.11) through (4.15).

$$E_x = -\frac{\beta_{x,m}\beta_{z,mn}}{\omega\mu\varepsilon}\cos(\beta_{x,m}x)\sin(\beta_{y,n}y)\left[B_{mn}^+ e^{-j\beta_{z,mn}z} + B_{mn}^- e^{+j\beta_{z,mn}z}\right] \tag{4.11}$$

$$E_y = -\frac{\beta_{y,n}\beta_{z,mn}}{\omega\mu\varepsilon}\cos(\beta_{y,n}y)\sin(\beta_{x,m}x)\left[B_{mn}^+ e^{-j\beta_{z,mn}z} + B_{mn}^- e^{+j\beta_{z,mn}z}\right] \tag{4.12}$$

$$E_z = -j\frac{\beta_{c,mn}^2}{\omega\mu\varepsilon}\sin(\beta_{y,n}y)\sin(\beta_{x,m}x)\left[B_{mn}^+ e^{-j\beta_{z,mn}z} + B_{mn}^- e^{+j\beta_{z,mn}z}\right] \tag{4.13}$$

$$H_x = \frac{\beta_{y,n}}{\mu}\cos(\beta_{y,n}y)\sin(\beta_{x,m}x)\left[B_{mn}^+ e^{-j\beta_{z,mn}z} + B_{mn}^- e^{+j\beta_{z,mn}z}\right] \tag{4.14}$$

$$H_y = -\frac{\beta_{x,m}}{\mu}\cos(\beta_{x,m}x)\sin(\beta_{y,n}y)\left[B_{mn}^{+}e^{-j\beta_{z,mn}z} + B_{mn}^{-}e^{+j\beta_{z,mn}z}\right] \tag{4.15}$$

Where $\beta_{x,m} = \frac{m\pi}{a}$, $\beta_{y,n} = \frac{n\pi}{b}$, and $\beta_{z,mn}$ matches equation (4.10). However, this work complements [1] and [2], which focus on dielectric samples constructed of UV cured polymer, and only the TE field configurations are analyzed. The UV cured polymer samples are displayed in Figure 42.

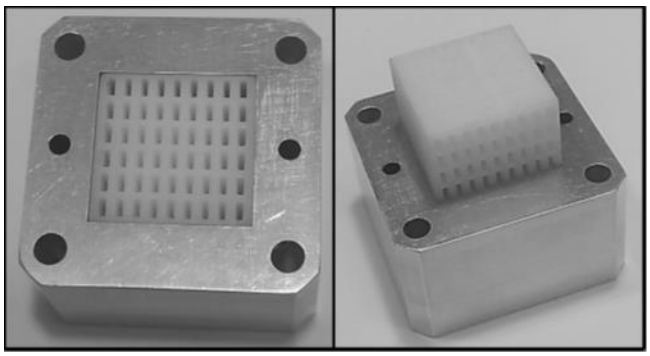

Figure 42. Polymer crystal within square PEC sample holder [2].

The end of Chapter III showed that the taper is indeed lossless for certain excitation modes. Therefore, for these lossless modes, the tapered transition should not attenuate the dominant excitation mode.

Figure 43 through Figure 46 show the electric field magnitude at $\Gamma_1$ for the low, middle, and high frequencies from the X-band excitation. Likewise, Figure 47 through Figure 49 show the electric field magnitude at $\Gamma_2$. The fields are as expected because the dominant contribution is $TE_{10}$.

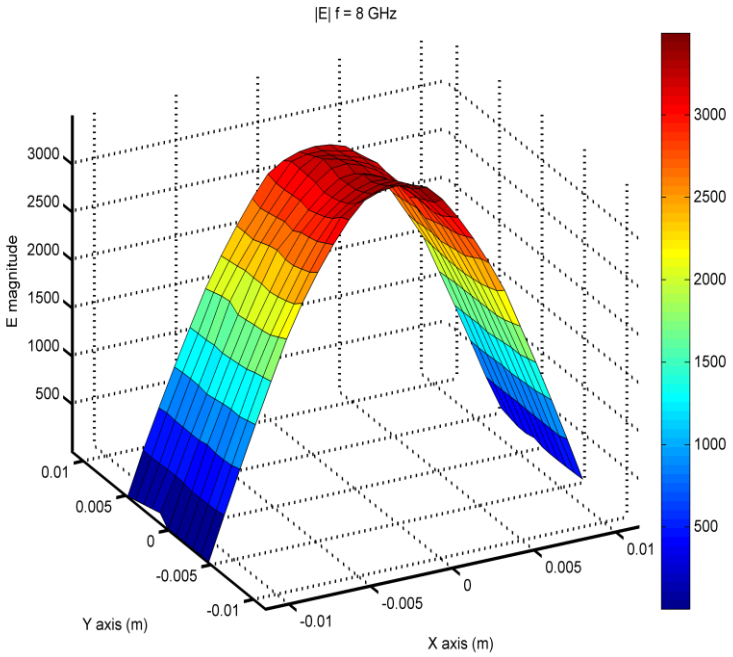


Figure 43. Electric field measured at $\Gamma_1$ at 8 GHz.

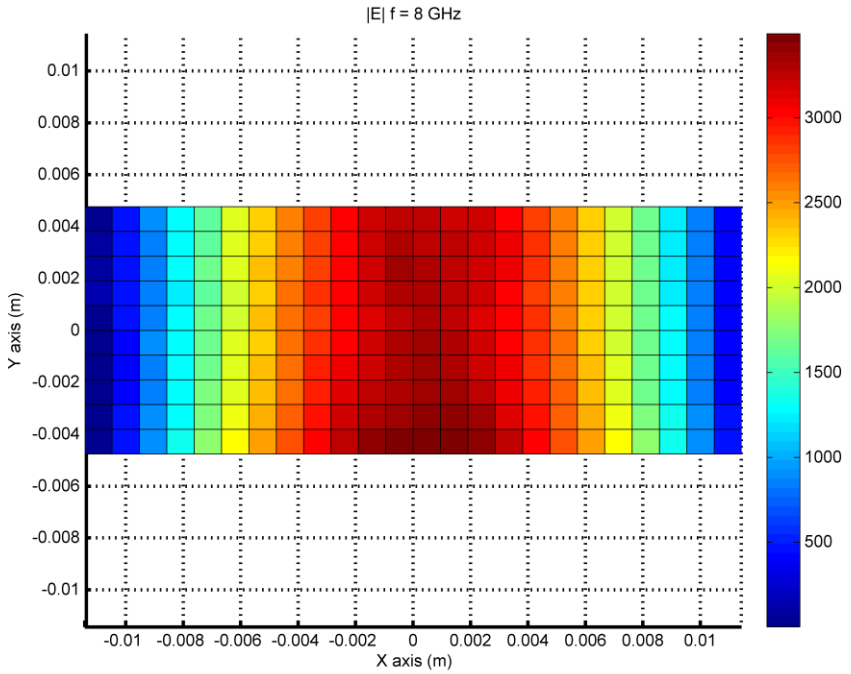


Figure 44. Electric field cross section (xy-plane) of $\Gamma_1$ at 8 GHz.

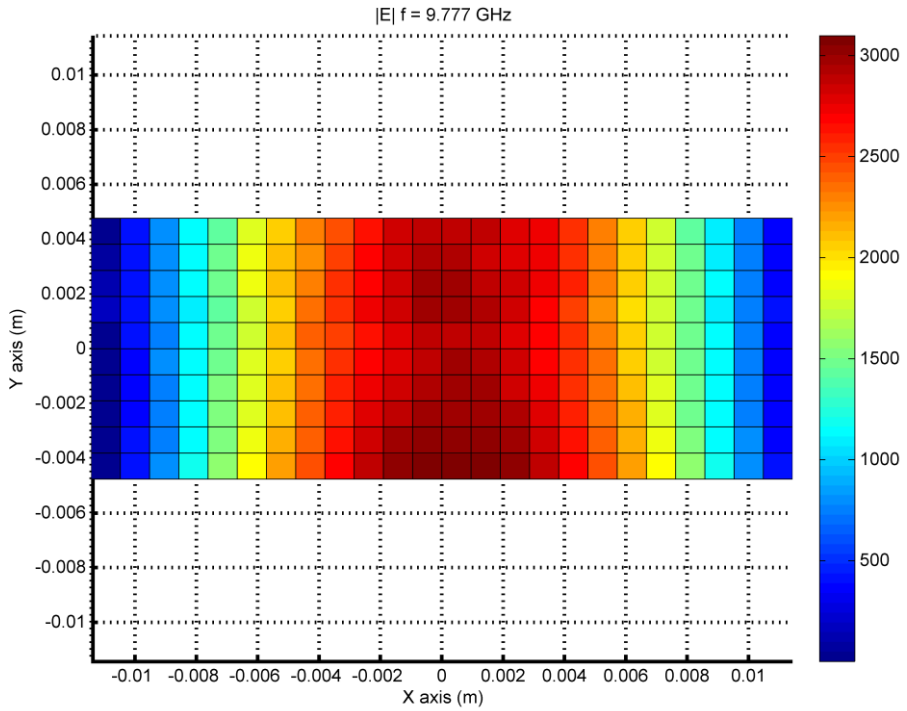


Figure 45. Electric field cross section of $\Gamma_1$ at 9.777 GHz.

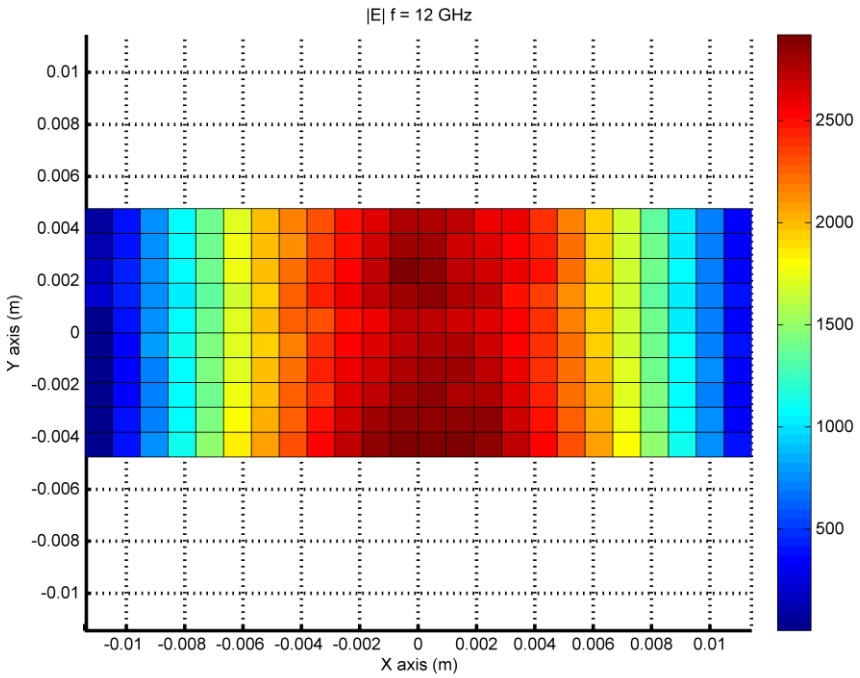


Figure 46. Electric field cross section of $\Gamma_1$ at 12 GHz.

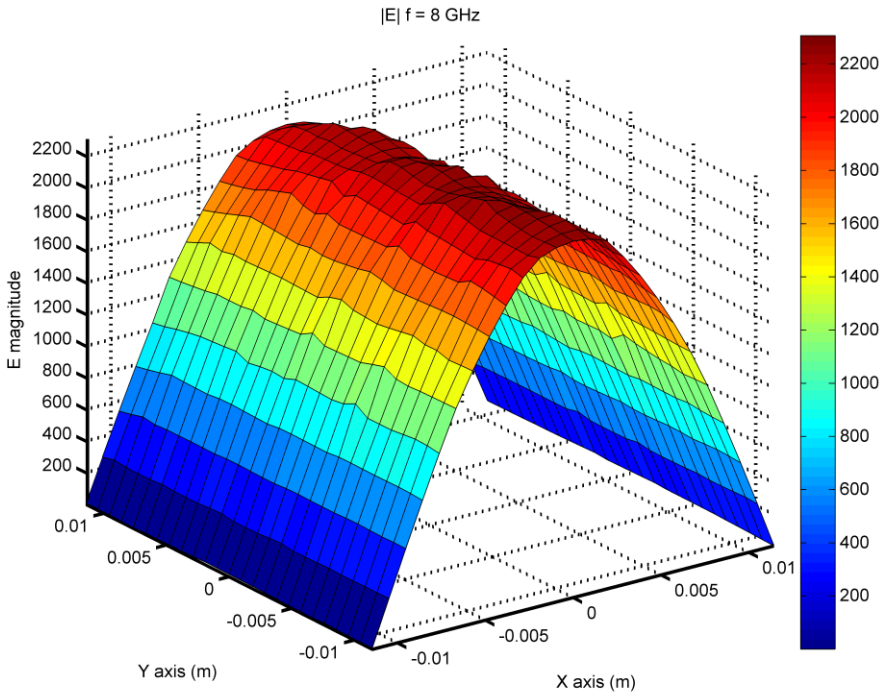


Figure 47. Electric field measured of $\Gamma_2$ at 8 GHz.

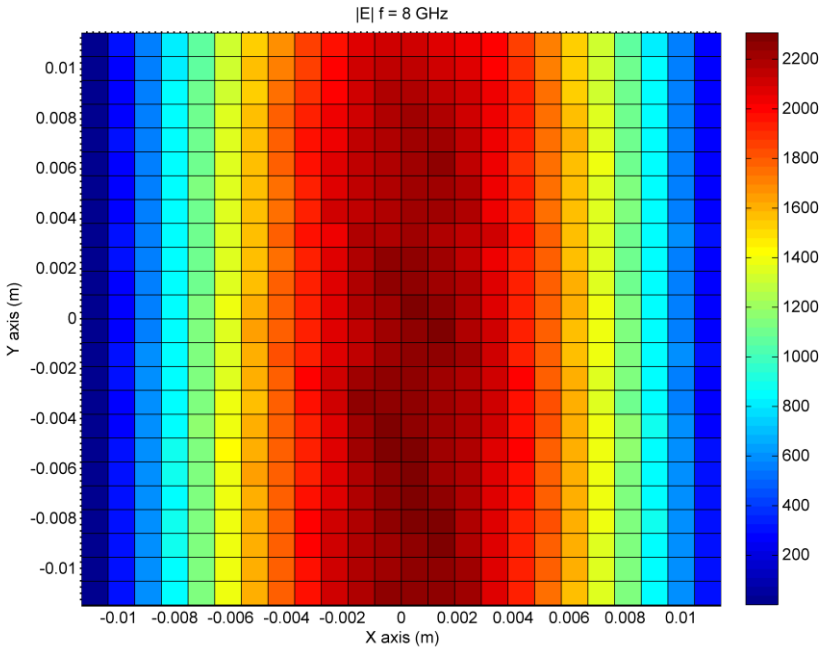


Figure 48. Electric field cross section of $\Gamma_2$ at 8 GHz.

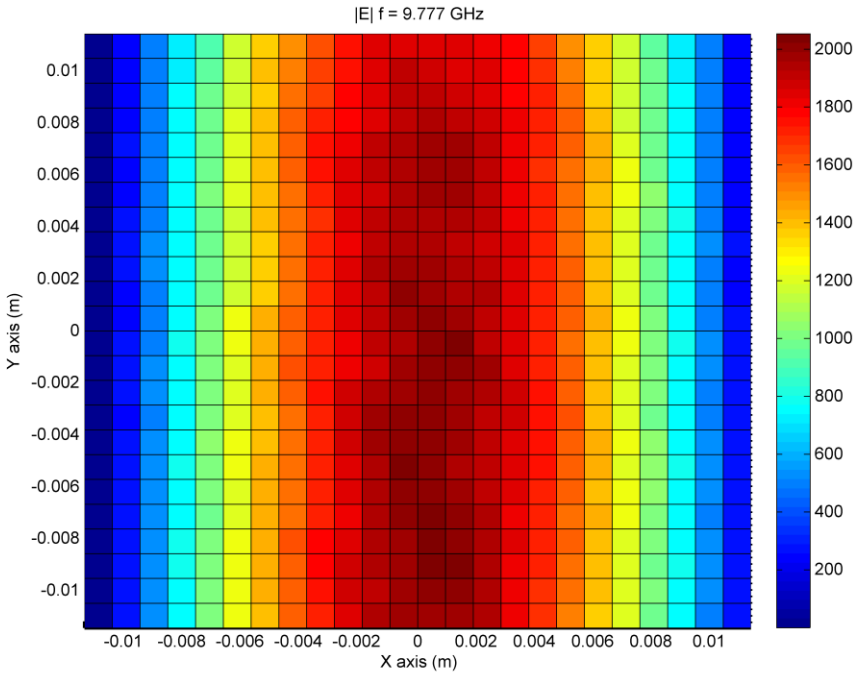


Figure 49. Electric field cross section at $\Gamma_2$ at 9.777 GHz.

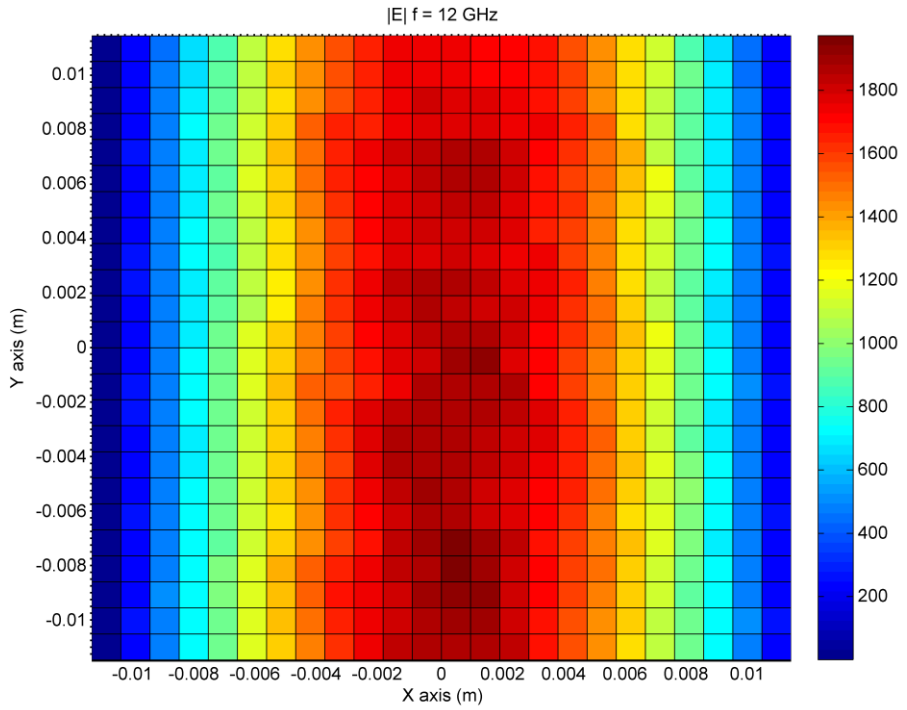


Figure 50. Electric field cross section of $\Gamma_2$ at 12 GHz.

Figure 47 through Figure 50 show that the dominant mode is preserved, yet as the higher frequencies in the X-band sweep are approached, we can see the magnitude of $\vec{E}_{10}$ at $\Gamma_2$ begins to diminish. This behavior could be caused by the generation of higher order modes within the transition section. However, as the tapered waveguide is lossless, higher order modes may propagate to the junction at $\Gamma_2$. Therefore, these modes must be preserved for the direct excitation at the sample region represented by Figure 41. But which higher order modes are present and form the total field at $\Gamma_2$?

Since the tapered transition was deemed lossless, all of the higher order modes which are excited within Section 2 (and thus reflect at the junction $\Gamma_2$) in Figure 40, will propagate back into Section 1. Therefore, if "listening" ports are inserted at $\Gamma_1$ to numerically calculate the response for certain $TE_{mn}$ modes induced within the taper, it should be possible to get an idea of the strongest contributing higher order modes.

To do this, the system in Figure 40 is excited at Port 1 by a $TE_{mn}$ mode. Then, five arbitrary listening ports are defined at the same plane as excitation (Port 1). However, each listening port performs a separate reaction integral to test for the specified mode. This reaction integral is defined as

$$\langle \mathbf{A}, \mathbf{B} \rangle_{\Gamma_n} = \iint \mathbf{B}^H \mathbf{A} \, d\Gamma_n \tag{4.11}$$

where $H$ denotes the Hermitian transpose. The reaction integral, when to define S-parameters, is a normalization on any boundary $d\Gamma_n$. This normalization must occur since $\Gamma_1$ and $\Gamma_2$ alter in dimension from rectangular to square. The reaction integral preserves the fact that only propagating and evanescing waves can exist within the guide. In other words, no energy larger than that induced into the system at Port 1 is able to propagate through the guide and reach Port 2. This is represented by equations (4.12) through (4.14) below. The scattering parameter at Port 1 can be represented as

$$S_{11} = \frac{\left\langle \mathbf{E}^{(1)} - \mathbf{E}_0^{(1)}, \mathbf{E}_0^{(1)} \right\rangle_{\Gamma_1}}{\left\langle \mathbf{E}_0^{(1)}, \mathbf{E}_0^{(1)} \right\rangle_{\Gamma_1}} = \frac{a^-}{a^+}\Big|_{e^-=0} \tag{4.12}$$

where $\mathbf{E}^{(1)}$ represents the total field on boundary $\Gamma_1$, $\mathbf{E}_0^{(1)}$ represents the dominant $TE_{10}$ mode excitation, and $e^-$is the excitation at Port 2. Utilizing the listening ports, Equation (4.12) can be used to solve for any desired mode on $\Gamma_1$ given an input of $\mathbf{E}_0^{(1)}$ as

$$S_{11}^{mn} = \frac{\left\langle \mathbf{E}^{(1)} - \mathbf{E}_0^{(1)}, \mathbf{E}_{mn}^{(1)} \right\rangle_{\Gamma_1}}{\left\langle \mathbf{E}_0^{(1)}, \mathbf{E}_0^{(1)} \right\rangle_{\Gamma_1}} = \frac{a^-}{a^+}\Big|_{e^-=0} \tag{4.13}$$

and will give insight to the number of modes which are able to propagate back through Section 2 and into Section 1. $\mathbf{E}_{mn}^{(1)}$ represents the electric field on boundary $\Gamma_1$ for the *mn*th mode given a $TE_{10}$ electric field excitation. Recall, the electric field configuration for $TE_{10}$ takes the form of Equation (4.1). Utilizing equation (4.13), Figure 51 shows the modal results for $TE_{10}$, $TE_{11}$, $TE_{20}$, $TE_{30}$, $TE_{50}$, $TE_{70}$.

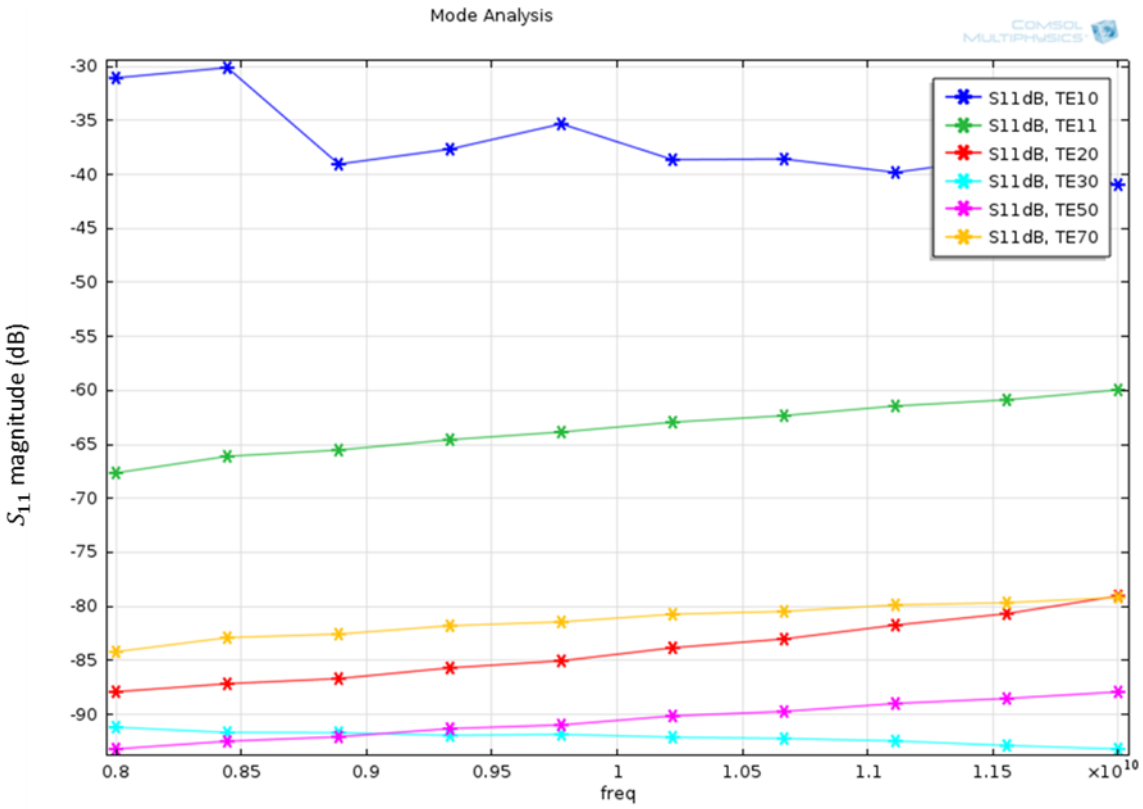


Figure 51. $S_{11}^{mn}$ magnitude at Port 1

The dominant $TE_{10}$ mode is preserved as expected, and the next highest contributor towards the fields measured at Port 1 is the $TE_{11}$ mode. The next strongest mode (3rd) is $TE_{70}$ followed by $TE_{20}$, $TE_{50}$, and $TE_{30}$ respectively.

The reaction integral for $S_{21}$ is.

$$S_{21} = \frac{\left\langle \mathbf{E}^{(2)}, \mathbf{E}_0^{(2)} \right\rangle_{\Gamma_2}}{\left\langle \mathbf{E}_0^{(1)}, \mathbf{E}_0^{(1)} \right\rangle_{\Gamma_1}} = \frac{e^+}{a^+}\bigg|_{e^-=0} \tag{4.14}$$

Where $\mathbf{E}^{(2)}$ represents the entire field on the boundary $\Gamma_2$ (Port 2), $\mathbf{E}_0^{(2)}$ represents the field entering Port 2, and $\mathbf{E}_0^{(1)}$ still represents the field leaving Port 1 ($TE_{10}$). Recalling the discussion on mode matching in Section 2.4, it is easy to see that the reaction integrals for $S_{11}$ and $S_{21}$ can be used to solve for modal amplitudes at any junction (equations (2.4.11) and (2.4.12)). This is explored further in Chapter V.

# CHAPTER 5

## CONCLUSIONS

### 5.1. Summary

The analysis in Chapter IV yielded which modes have a contributing factor to the response measured at the sample region ($\Gamma_2$). Since we have an idea of the strongest contributing modes, the methods presented in Chapter II can be utilized to excite the sample region directly without simulation of the WR-90 or transition guide as seen in Figure 51. These methods include the *T*-matrix approach or the mode matching solution.

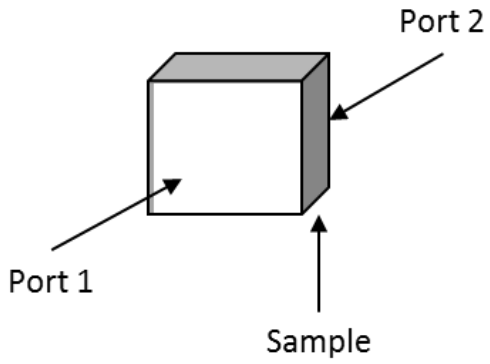


Figure 52. Reduced model.

The mode matching approach would utilize all the data collected in the $TE_{mn}$ analysis of the tapered transition in section 3.5.2 (Figures 28 through 31) and Chapter IV (Figure 50).

The reaction integral for $S_{11}$ is derived from three electric field evaluations; the total field $\mathbf{E}^{(1)}$, the excitation $\mathbf{E}_0^{(1)}$, and the scattered field (equation (5.1)).

$$\boldsymbol{E}^{scattered} = \mathbf{E}^{(1)} - \mathbf{E}_0^{(1)} \tag{5.1}$$

The scattered electric field is simply a measure of the entire field at a Port minus the excitation from that port. In other words, the scattered field used in $S_{11}$ measurement is simply the reflected waves caused at junctions $\Gamma_1$ and $\Gamma_2$ which do not evanesce before reaching Port 1 in Figure 40 ($a^-$and $b^-$) . Coupling this with the discussion on mode matching in section 2.4, we are able to model the scattered field in terms of any higher order propagating modes as seen in equation (5.2)

$$\boldsymbol{E}^{scattered} = \sum_{m,n}^{\infty} A_{mn}^{(-)} \boldsymbol{e}_{nm}^{(1)}(x,y)\, e^{+j\beta_{mn}^{(1)} z} \tag{5.2}$$

where $A_{mn}^{(-)}$ is the amplitude of the reflected wave per mode, $\boldsymbol{e}_{nm}^{(1)}(x,y)$ is the eigenfunction per mode, and $\beta_{mn}^{(1)}$ is the propagation constant per mode. The superscript (1) denotes the region of interest and will vary from air filled in sections 1 and 2 to anisotropic in section 3 of Figure 40.

Using the analysis done in Chapter IV, specifically Figure 50, one is able to expand equation (5.2) in terms of the strongest four modes: $TE_{10,}$ $TE_{11}$, $TE_{70}$, and $TE_{20}$.

$$\boldsymbol{E}^{scattered} = A_{10}^{(-)}\boldsymbol{e}_{10}^{(1)}e^{+j\beta_{10}^{(1)}z} + A_{11}^{(-)}\boldsymbol{e}_{11}^{(1)}e^{+j\beta_{11}^{(1)}z} + A_{70}^{(-)}\boldsymbol{e}_{70}^{(1)}e^{+j\beta_{70}^{(1)}z} + A_{20}^{(-)}\boldsymbol{e}_{20}^{(1)}e^{+j\beta_{20}^{(1)}z} \tag{5.3}$$

where

$$\boldsymbol{e}_{10}^{(1)} = \sin\left(\frac{\pi}{a}x\right) \tag{5.4}$$

$$\boldsymbol{e}_{11}^{(1)} = \sin\left(\frac{m\pi}{a}x\right)\cos\left(\frac{n\pi}{b}y\right) = \sin\left(\frac{\pi}{a}x\right)\cos\left(\frac{\pi}{b}y\right) \tag{5.5}$$

$$\boldsymbol{e}_{70}^{(1)} = \sin\left(\frac{m\pi}{a}x\right)\cos\left(\frac{n\pi}{b}y\right) = \sin\left(\frac{7\pi}{a}x\right) \tag{5.6}$$

$$\boldsymbol{e}_{20}^{(1)} = \sin\left(\frac{m\pi}{a}x\right)\cos\left(\frac{n\pi}{b}y\right) = \sin\left(\frac{2\pi}{a}x\right) \tag{5.7}$$

Recalling equation (2.4.11)

$$S_{11}(p) = \frac{\sum_{m=1}^{\infty} A_m^-}{A_p^+}$$

we can see that the $S_{11}$ value is simply the ratio of reflected waves to that of the excitation. In equation (2.4.11) the excitation is the forward going $p^{th}$ mode, however, only the $TE_{10}$ mode is excited at Port 1, so (2.4.11) will become

$$S_{11}^m = \frac{\sum_{m=1}^{4} A_m^-}{A_{10}^+} \tag{5.8}$$

where $\sum_{m=1}^{4} A_m^-$ represents the sum of the first four higher order modes which are reflected at $\Gamma_1$ and $\Gamma_2$. Utilizing equation (5.8) and multiplying equation (5.3) by the excitation amplitude of $A_{10}^+$ will yield:

$$\boldsymbol{E}^{scattered} = \left[S_{11}^{(\mathrm{TE}_{10})}\boldsymbol{e}_{10}^{(1)}e^{+j\beta_{10}^{(1)}z} + S_{11}^{(\mathrm{TE}_{11})}\boldsymbol{e}_{11}^{(1)}e^{+j\beta_{11}^{(1)}z}\right. \tag{5.9}$$

$$\left. + S_{11}^{(\mathrm{TE}_{70})}\boldsymbol{e}_{70}^{(1)}e^{+j\beta_{70}^{(1)}z} \quad + S_{11}^{(\mathrm{TE}_{20})}\boldsymbol{e}_{20}^{(1)}e^{+j\beta_{20}^{(1)}z}\right] \cdot A_{10}^{(+)}$$

This scattered field will be the new excitation into the sample region as shown in Figure 41.

The only down side to this approach is the need for numerical data exports from simulation to determine the propagation constants per mode $\beta_{mn}^{(1)}$. An alternative approach would be to utilize the *T*-matrix. Since the *T*-matrix allows us to solve for the incoming and outgoing waves at any junction of the "multi-waveguide" cascaded system shown in Figure 52, we are able to solve how individual modes propagate through the tapered transition.

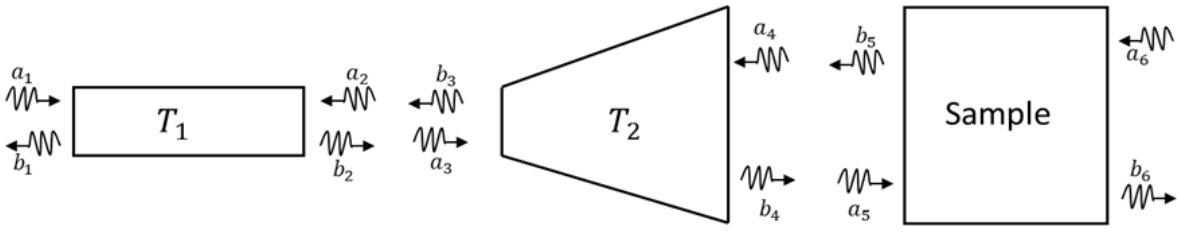


Figure 53. *T*-matrix representation of Figure 40.

Following the discussion in Chapter II, we are able to cascade the air filled portions of the RTST guide to solve for the outgoing wave ($b_4$) into the sample region as seen in Figure 53.

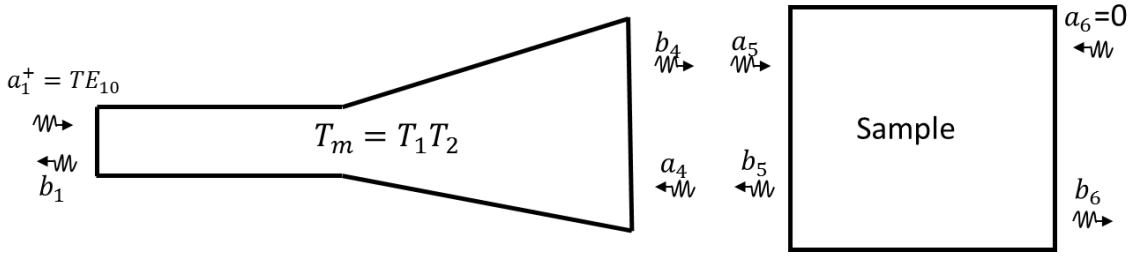


Figure 54. *T*-matrix cascade applied to Figure 40.

This cascaded section of waveguide, $T_m$, relates the incoming $TE_{10}$ wave to the output of the tapered transition ($b_4 = a_5$) for the given excitation mode. To solve for the tapered transitions net response, a *T*-matrix solution must be obtained per mode. The linear system of equations which defines the *T*-matrix (equation (2.3.1)) can be rearranged to solve for the desired wave input to the sample region ($b_4$).

$$\begin{bmatrix} a_1 \\ b_1 \end{bmatrix} = [T^m] \begin{bmatrix} b_4 \\ a_4 \end{bmatrix} \tag{5.10}$$

$$a_1 = T_{11}^m b_4 + T_{12}^m a_4 \tag{5.11}$$

$$b_1 = T_{21}^m b_4 + T_{22}^m a_4 \tag{5.12}$$

Solving equation (5.11) and (5.12) for the incoming wave to the sample region yields:

$$b_4 = \frac{a_1 - T_{12}^m a_4}{T_{11}^m} \tag{5.13}$$

$$b_4 = \frac{b_1 - T_{22}^m a_4}{T_{21}^m} \tag{5.14}$$

Since we are only exciting Port 1 with the dominant $\mathrm{TE}_{10}$ wave, $a_1 \sim \mathrm{TE}_{10}$ and $a_4 = 0$. Also, we know that the reflected waves seen at Port 1 ($b_1$) will consist of all the higher order modes reflected from $\Gamma_1$ and $\Gamma_2$. Therefore, we able to redefine equations (5.11) and (5.12) as:

$$b_4 = \frac{a_1}{T_{11}^m} = \frac{\mathrm{TE}_{10}}{T_{11}^m} \tag{5.15}$$

$$b_4 = \frac{\sum \mathrm{TE}_{mn}}{T_{21}^m} \tag{5.16}$$

Recalling equations (2.3.2) through (2.3.5) we are able to model the incoming waves to the sample region in terms of the *S*-parameters by converting the *T*-parameters appropriately. This is shown in equations (5.17) and (5.18)

$$b_4 = \mathrm{TE}_{10} \cdot S_{21}^m \tag{5.17}$$

$$b_4 = \frac{\sum \mathrm{TE}_{mn} \cdot S_{21}^m}{S_{11}^m} \tag{5.18}$$

### 5.2. Recommendations for future work

If we were to study more complex samples such as fully anisotropic or ferromagnetic materials, we will find that the $\mathrm{TE}_{mn}$ only solution to Maxwell's equation does not hold.

This behavior stems from the fact that the anisotropic or ferromagnetic sample has a magnetic response represented by its permeability tensor $\bar{\bar{\mu}}$. It is safe to assume that this magnetic response will excite $TM_{mn}$ modes within the sample region. Field distributions for $TM_{mn}^{z}$ modes within a bounded PEC structure are previously shown, but are relisted below [3]:

$$E_x = -\frac{\beta_{x,m}\beta_{z,m}}{\omega\mu\varepsilon}\cos(\beta_{x,m}x)\sin(\beta_{y,n}y)\left[B_{mn}^{+}e^{-j\beta_{z,m}z} + B_{mn}^{-}e^{+j\beta_{z,m}z}\right] \tag{5.2.1}$$

$$E_y = -\frac{\beta_{y,n}\beta_{z,m}}{\omega\mu\varepsilon}\cos(\beta_{y,n}y)\sin(\beta_{x,m}x)\left[B_{mn}^{+}e^{-j\beta_{z,m}z} + B_{mn}^{-}e^{+j\beta_{z,m}z}\right] \tag{5.2.2}$$

$$E_z = -j\frac{\beta_{c,mn}^{2}}{\omega\mu\varepsilon}\sin(\beta_{y,n}y)\sin(\beta_{x,m}x)\left[B_{mn}^{+}e^{-j\beta_{z,m}z} + B_{mn}^{-}e^{+j\beta_{z,m}z}\right] \tag{5.2.3}$$

$$H_x = \frac{\beta_{y,n}}{\mu}\cos(\beta_{y,n}y)\sin(\beta_{x,m}x)\left[B_{mn}^{+}e^{-j\beta_{z,m}z} + B_{mn}^{-}e^{+j\beta_{z,m}z}\right] \tag{5.2.4}$$

$$H_y = -\frac{\beta_{x,m}}{\mu}\cos(\beta_{x,m}x)\sin(\beta_{y,n}y)\left[B_{mn}^{+}e^{-j\beta_{z,m}z} + B_{mn}^{-}e^{+j\beta_{z,m}z}\right] \tag{5.2.5}$$

where $\beta_{x,m}$ and $\beta_{y,m}$ will be determined from boundary conditions and mode number. If the sample is biaxial anisotropic and made from a magnetically responsive material, the propagation constant $\beta_{z,m}$ is related to the constitutive parameters of the sample region such that [2]

$$\beta_{z,m} = \pm\sqrt{\omega^2\varepsilon_x\mu_y - \frac{\varepsilon_x}{\varepsilon_z}\beta_{x,m}^{2}} \tag{5.2.6}$$

Future work will also include an intensive comparison between the solutions obtained by the proposed methods in section 5.1 and the numerical solutions obtained by the full wave modeling and simulation.

## REFERENCES


[1] A. Knisely, M. Havrilla, P. Collins, M. Hyde, A. Bogle, J. Allen, and E. Rothwell, "Biaxial anisotropic material characterization using rectangular to square waveguide," *36th Annual Antenna Measurement & Techniques Association Symposium*, Oct. 2014.

[2] A. G. Knisely, *Biaxial Anisotropic Material Development and Characterization Using Rectangular To Square Waveguide*, M.S. Thesis, Air Force Institute of Technology, Mar. 2015.

[3] David. M. Pozar, *Microwave Engineering*, 4th ed. NJ: Wiley, 2012, pp. 184-210.

[4] C. Balanis, *Advanced Engineering Electromagnetics*, 2nd ed. USA: Wiley, pp. 352-360.

[5] B. Crowgey, O. Tuncer, J. Tang, E. Rothwell, B. Shanker, L. Kempel, and M. Havrilla, "Characterization of biazial anisotropic material using a reduced aperture waveguide," *IEEE Transactions on Instrumentation and Measurement*, vol. 62, no. 10, pp. 2739-2750, Oct. 2013.

[6] Dean A. Frickey, "Conversions Between S, Z, Y, h, ABCD, and T Parameters which are Valid for Complex Source and Load Impedances," *IEEE Transactions on Microwave Theory and Techniques*, vol. 42, no. 2, pg. 205-211, Feb. 1994.

[7] J. Brand, "Biaxial Material Design Method for the Reduced Aperture Waveguide Model," M.S Thesis, Wright State University, Dec. 2014.

[8] COMSOL Multiphysics. URL: http://www.comsol.com.

[9] P. Nikitin, D. Stancil, E. Erosheva, "Estimating the Number of Modes in Multimode Waveguide Propagation Environment," *Antennas and Propagation, 2011 IEEE International Symposium*, vol. no. pp.1662,1665, 3-8 Jul. 2011.

[10] L. Solymar, "Spurious Mode Generation in Nonuniform Waveguide," *IRE Transactions on Microwave Theory and Techniques*, vol. 7, no.3, pp.379-383, Jul. 1959.

[11] Mark M. Scott, Daniel L. Faircloth, Jeffrey A. Bean, and Samuel G. Holliday, "Biaxial Permittivity Determination for Electrically Small Material Specimens of Complex Shape Using Shorted Rectangular Waveguide Measurements," *IEEE Transactions on Instrumentation and Measurement*, vol. 63, no.4, Apr. 2014.

[12] Dorey, S.P.; Havrilla, M.J.; Frasch, L.L.; Choi, C.; Rothwell, E.J., "Stepped-waveguide material-characterization technique," *Antennas and Propagation Magazine, IEEE* , vol.46, no.1, pp.170,175, Feb. 2004.

[13] Itoh, Tatsuo, "The Finite Element Method," in *Numerical Techniques for Microwave and Millimeter-wave Passive Structures,* New York, NY: Wiley, 1989, ch. 2, pp. 33-133.

[14] L.N. Dworsky, *Introduction to Numerical Electrostatics Using MATLAB,* Hoboken, NJ: Wiley, 2014, ch. 12, pp. 265-288.

[15] De-embedding Techniques in Advanced Design System, Technical notes, Agilent Technologies, Santa Clara, CA, pp. 8-14.

[16] Y. C. Shih, K. G. Gray, "Convergency of numerical solutions of step-type waveguide discontinuity problems by modal analysis," *IEEE MTT-S Int. Microwave Symp. Dig.*, pp. 233-235, May 1983.

[17] P. Rizzi, "S-Parameters and Signal Flow Graphs," in *Microwave Engineering Passive Circuits,* Enlegwood Cliffs, NJ: Prentice Hall, 1988, ch 4, pp. 168-191.

[18] B. Smith, M.H. Carpentier, *The Microwave Engineering Handbook Vol 1,* New York, NY: Van Nostrand Reinhold, 1993.